Available online at www.sciencedirect.com
ScienceDirect
Journal of Computational Physics 227 (2008) 6001–6043
JOURNAL OF COMPUTATIONAL PHYSICS
www.elsevier.com/locate/jcp

Multi-dimensional limiting process for three-dimensional flow physics analyses

Sung-Hwan Yoon [a], Chongam Kim [a,b,*], Kyu-Hong Kim [a]

[a] School of Mechanical and Aerospace Engineering, Seoul National University, Seoul 151-742, Republic of Korea
[b] Institute of Advanced Aerospace Technology, School of Mechanical and Aerospace Engineering, Seoul National University, Seoul, Republic of Korea

Received 15 May 2007; received in revised form 22 November 2007; accepted 13 February 2008
Available online 23 February 2008

Abstract

The present paper deals with an efficient and accurate limiting strategy for multi-dimensional compressible flows. The multi-dimensional limiting process (MLP) which was successfully proposed in two-dimensional case [K.H. Kim, C. Kim, Accurate, efficient and monotonic numerical methods for multi-dimensional compressible flows. Part II: Multi-dimensional limiting process, J. Comput. Phys. 208 (2) (2005) 570–615] is modified and refined for three-dimensional application. For computational efficiency and easy implementation, the formulation of MLP is newly derived and extended to three-dimensional case without assuming local gradient.

Through various test cases and comparisons, it is observed that the newly developed MLP is quite effective in controlling numerical oscillation in multi-dimensional flows including both continuous and discontinuous regions. In addition, compared to conventional TVD approach, MLP combined with improved flux functions does provide remarkable increase in accuracy, convergence and robustness in steady and unsteady three-dimensional compressible flows.

PACS: 47.11.Df; 47.40.Ki; 47.85.Gj

Keywords: Multi-dimensional limiting condition; Multi-dimensional limiter; High-speed compressible flows; TVD condition; Numerical oscillation

1. Introduction

During the past few decades, many ways to control numerical oscillation have been explored, and several limiting concepts have been proposed. Most remarkable progress would be TVD, TVB and ENO/WENO. The concept of total variation diminishing (TVD) was proven to be extremely successful in solving hyperbolic conservation laws [1,2]. The TVD criterion provides a fundamental idea for oscillation control and is still very popular, but conventional TVD schemes could yield somewhat unsatisfactory performance near extrema.

* Corresponding author. Tel.: +82 2 880 1915; fax: +82 2 887 2662.
E-mail address: chongam@snu.ac.kr (C. Kim).

0021-9991/$ - see front matter © 2008 Elsevier Inc. All rights reserved.
doi:10.1016/j.jcp.2008.02.012

Essentially non-oscillatory (ENO) [3–5], and weighted essentially non-oscillatory (WENO) [6–9] approaches were proposed to cure the defect by exploiting local adaptive stencils, and the concept of total variation bounded (TVB) [10] was introduced to relax clipping across extrema. Although TVB or ENO/WENO avoids unphysical clipping and thus enhances accuracy, numerical oscillation and/or instability are frequently observed especially in multi-dimensional flow analyses which in turn badly influence on solution accuracy and convergence. As successive studies, MP limiter [11] and ENO/WENO filters [12,13] have also been developed in recent years. All of these approaches are, one way or another, related to the treatment of limiting or filtering of numerical fluxes to yield oscillation-free solutions without compromising solution accuracy.

Most oscillation-free schemes developed so far are mainly based on the mathematical analysis of one-dimensional convection equation, and applied to systems of equations with some linearization step. After that, they are usually extended to multi-dimensional flow by dimensional splitting. Though this approach may work successfully in many cases, it is often insufficient or almost impossible to control oscillation near shock discontinuity in multi-dimensional flow. Thus, the need to explore an oscillation control method for multi-dimensional applications is manifest.

One of the fundamental difficulties in handling multi-dimensional problems is to define monotonic property. Especially, the definition of monotonic distribution is ambiguous near saddle point [14]. In addition, Goodman and LeVeque showed TVD scheme in two-space dimensions can not be more than first-order accurate [15]. Thus, it looks pessimistic to develop an oscillation control scheme with global higher order accuracy in multi-space dimensions.

In order to find out a suitable criterion for oscillation control in multi-dimensional flows, Kim and Kim extended the one-dimensional monotonic condition to two-dimensional flow, and successfully presented the two-dimensional limiting condition [16]. With the limiting condition, a multi-dimensional limiting process (MLP) is proposed which shows enhanced accuracy and convergence characteristics for the two-dimensional compressible Euler and Navier–Stokes equations. The present work is continuation of our efforts to arrive at a multi-dimensional limiting process (MLP). The idea of MLP is more refined so that it can be efficiently implemented in three-dimensional practical applications.

Despite successful performance of MLP scheme in two-dimensional compressible flow, the three-dimensional extension is not straightforward at all due to its complexity in satisfying the multi-dimensional limiting condition in three-dimensional flow. The extension based on dimensional splitting manner can not be applied in this case. Since the MLP formulation includes the ratio of physical variation in one coordinate direction to the others, it needs to be newly derived so that the final form is proper for three-dimensional situation. In this work, we firstly present a newly formulated MLP in two-dimensional case and then it is extended to three-dimensional case.

The present paper is organized as follows. After a brief description of the original MLP for two-dimensional compressible flow in Section 2.1, we discuss the limiting characteristics of MLP in Section 2.2, and difficulties in three-dimensional extension are going to be mentioned in Section 2.3. In Sections 3.1 and 3.2, we derive a newly formulated MLP scheme for two- and three-dimensional flow, respectively. And then, the detailed implementation procedure is summarized in Section 3.3. In Section 4, extensive test cases are presented to verify characteristics and performance of MLP for two- and three-dimensional compressible flow. Finally, conclusion is given in Section 5.

2. Review of MLP for two-dimensional flow

In this section, MLP for two-dimensional compressible flow which is originally proposed by Kim and Kim [16] is briefly reviewed. Additionally, several characteristics of MLP scheme are also examined. As a starting point, we explain the basic concept of MLP by comparing it with TVD MUSCL approach.

2.1. Basic concept of MLP: MLP vs. TVD MUSCL limiters

According to the Godunov-type approach, steps to construct a numerical flux at a cell-interface usually consist of interpolation stage and evolution stage. Interpolation stage is generally decoupled from evolution stage where a local Riemann problem is solved at a cell-interface. To obtain a higher spatial approximation, it is sufficient to modify interpolation stage without modifying a Riemann solver. Referring that piecewise

constant state generates the first-order spatial accuracy, piecewise linear or quadratic distribution is applied to obtain the second- or the third-order spatial accuracy. This philosophy to obtain second-order upwind schemes is often referred as the MUSCL approach [17].

Based on the MUSCL approach with TVD limiter, cell-interface states are written as follows:

$$q^{\mathrm{L}}_{i+1/2} = \hat{q}_i + \frac{1}{4}\left[(1-\kappa)\phi(r_{\mathrm{L}}) + (1+\kappa)r_{\mathrm{L}}\phi\left(\frac{1}{r_{\mathrm{L}}}\right)\right]\Delta\hat{q}_{i-1/2}, \tag{1}$$

$$q^{\mathrm{R}}_{i+1/2} = \hat{q}_{i+1} - \frac{1}{4}\left[(1-\kappa)\phi(r_{\mathrm{R}}) + (1+\kappa)r_{\mathrm{R}}\phi\left(\frac{1}{r_{\mathrm{R}}}\right)\right]\Delta\hat{q}_{i+3/2}, \tag{2}$$

where q is a scalar component of primitive variable vector and $\hat{q}_i$ is the averaged value of q in the ith cell. Also, $\Delta\hat{q}_{i-1/2} = \hat{q}_i - \hat{q}_{i-1}$, $r_{\mathrm{L}} = \frac{\Delta\hat{q}_{i+1/2}}{\Delta\hat{q}_{i-1/2}}$ and $r_{\mathrm{R}} = \frac{\Delta\hat{q}_{i+1/2}}{\Delta\hat{q}_{i+3/2}}$. With $\kappa = \frac{1}{3}$, it achieves the third-order spatial accuracy and stencil is the same as central scheme. ϕ is a limiter function, which monitors a local gradient and determines a local slope under the TVD constraint. As is well-known, when TVD limiter is symmetric, Eqs. (1) and (2) are independent of κ, and they are simplified as follows:

$$q^{\mathrm{L}}_{i+1/2} = \hat{q}_i + \frac{1}{2}\phi(r_{\mathrm{L}})\Delta\hat{q}_{i-1/2}, \tag{3}$$

$$q^{\mathrm{R}}_{i+1/2} = \hat{q}_{i+1} - \frac{1}{2}\phi(r_{\mathrm{R}})\Delta\hat{q}_{i+3/2} \tag{4}$$

with the condition of $\frac{\phi(r)}{r} = \phi(\frac{1}{r})$.

One-dimensional limiting condition using the TVD constraint is written as in Ref. [2].

$$0 \leqslant \phi(r) \leqslant \min(2r, 2). \tag{5}$$

A TVD limiter which satisfies Eq. (5) can be defined as

General β-limiters

$$\phi(r) = \max(0, \min(\beta r, 1), \min(r, \beta)). \tag{6}$$

With $\beta = 1, 2$, Eq. (6) becomes minmod and superbee limiter, respectively. Since spurious oscillation is created when local slope in a cell becomes greater than differences of adjacent mean values, the TVD constraint, Eq. (5), could be interpreted as requiring that interface value should remain between adjacent cell-average values to avoid numerical oscillation. Mathematical analyses to support the TVD constraint are rigorous. However, when TVD concept is extended to multi-dimensional flow by dimensional splitting manner, it does not guarantee monotonic solutions.

In order to reinforce oscillation control in multi-dimensional flow, the multi-dimensional limiting process (MLP) was proposed [16] by which multi-dimensional flow features could be incorporated within the TVD framework. The basic formulation of MLP could be simply expressed as follows.

$$0 \leqslant \phi(r) \leqslant \min(\alpha r, \alpha), \tag{7}$$

where α is the multi-dimensional restriction coefficient which determines the baseline limiting region (see Fig. 1). The fundamental difference between Eqs. (5) and (7) is that TVD limiting region is fixed while MLP limiting region is varying according to multi-dimensional flow physics.

Depending on the choice of β, MLP in Eq. (7) shares some similarity with β-limiter in Eq. (6). The intrinsic difference is that β in Eq. (6) is arbitrarily predetermined by users, while α in Eq. (7) is evaluated according to multi-dimensionally distributed flow property during CFD computation. Thus, rationale in determining α would be the key point in MLP limiting. As a similar approach, a multi-dimensional monotonic condition for steady flow was proposed by Spekreijse, and a second-order monotone upwind scheme satisfying the condition was derived [18]. However, this approach has several defects. Firstly, it is only for steady state. Secondly, neighboring stencil is not fully exploited, and finally there is unknown parameter to be determined. Multi-dimensional limiters based on Spekreijse's monotonic condition have been developed by Barth [19–21] and Venkatakrishnan [22] particularly for unstructured grid. The MLP approach, however, does not necessarily depend on grid topology.

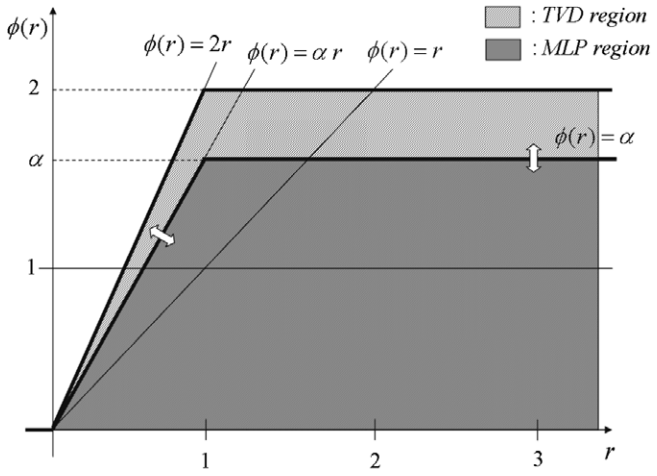

Fig. 1. Baseline MLP region; α is not a constant but a variable parameter which is evaluated according to multi-dimensional flow situation during CFD computation.

Following Ref. [16], the limiting condition in multi-space dimensions could be expressed as

$$\hat{q}^{\min}_{\text{neighbor}} \leqslant q \leqslant \hat{q}^{\max}_{\text{neighbor}}, \tag{8}$$

where q is a vertex point, and $\left(\hat{q}^{\min}_{\text{neighbor}}, \hat{q}^{\max}_{\text{neighbor}}\right)$ are the minimum and maximum cell-averaged values among neighboring candidates. Unlike one-dimensional flow, there are cell-vertex point as well as cell-center point in multi-dimensional flow. Thus, a limiting strategy considering both points would be essential. Compared with Eq. (8), one-dimensional TVD constraint does not possess any information on the distribution of flow features at cell-vertex point, which is important when flow gradient is not aligned with grid lines. The multi-dimensional limiting condition of Eq. (8) is very similar to Barth's choice [19]. However, there are several differences between Barth's limiter and MLP limiting, which will be discussed in next subsection.

By estimating vertex point values from one-dimensional monotonic interpolation, the proper range of α satisfying Eq. (8) can be derived as

$$1 \leqslant \alpha \leqslant \min\left[2, \frac{2\max(1, r_{L,j})\left(1+\max\left(0, \frac{\tan\bar{\theta}_{j+1}}{r_{R,j+1}}\right)\right)}{(1+\tan\tilde{\theta}_j)}\right], \tag{9}$$

where $\tan\tilde{\theta}_j = \frac{\Delta\hat{q}^+_x}{\Delta\hat{q}^+_y}$, $\tan\bar{\theta}_j = \frac{\Delta\hat{q}_{i+1/2,j}}{\Delta\hat{q}_{i,j+1/2}}$ and $\Delta\hat{q}^+_{x,y}$ are variations from center point to cell-interface. If we choose the maximum value of α, the multi-dimensional limiting function is obtained. For more detailed explanation, see Ref. [16]. Once the region for multi-dimensional limiting is determined, the next step is to obtain an actual slope. Improper choice of a local slope would yield dissipative or entropy-violating results such as minmod or superbee limiter. Assuming an optimal variation as

$$q_{i+1/2}|_{\text{optimal}} = \hat{q}_i + \frac{1}{2}\beta\Delta\hat{q}_{i-1/2}, \tag{10}$$

β is determined by the third-order or the fifth-order polynomial interpolation as follows:

MLP with the third order interpolation (MLP3):

$$\beta_{\text{L}} = \frac{1+2r_{L,i}}{3}, \quad \beta_{\text{R}} = \frac{1+2r_{R,i+1}}{3}. \tag{11}$$

MLP with the fifth-order interpolation (MLP5):

$$\beta_{\text{L}} = \frac{-2/r_{L,i-1}+11+24r_{L,i}-3r_{L,i}r_{L,i+1}}{30}, \tag{12}$$

$$\beta_{\mathrm{R}} = \frac{-2/r_{R,i+2} + 11 + 24r_{R,i+1} - 3r_{R,i+1}r_{R,i}}{30}. \tag{13}$$

Finally, the local slope β is filtered by the MLP condition of Eqs. (7) and (8) as

$$\phi(r) = \max(0, \min(\alpha, \alpha r, \beta)). \tag{14}$$

And, the left and right cell-interface values are obtained as follows:

$$q^{\mathrm{L}}_{i+1/2} = \hat{q}_i + \frac{1}{2}\max(0, \min(\alpha_{\mathrm{L}} r_{L,i}, \alpha_{\mathrm{L}}, \beta_{\mathrm{L}}))\Delta\hat{q}_{i-1/2}, \tag{15}$$

$$q^{\mathrm{R}}_{i+1/2} = \hat{q}_{i+1} - \frac{1}{2}\max(0, \min(\alpha_{\mathrm{R}} r_{R,i+1}, \alpha_{\mathrm{R}}, \beta_{\mathrm{R}}))\Delta\hat{q}_{i+3/2}. \tag{16}$$

2.2. MLP limiting and the maximum principle

In order to examine the relation between MLP schemes and the maximum principle, let us consider scalar conservation law in two-dimensional space.

$$\frac{\partial u}{\partial t} + \frac{\partial}{\partial x} f(u) + \frac{\partial}{\partial y} g(u) = 0. \tag{17}$$

Characteristics of MLP limiting can be readily shown by taking a similar step in the proof given by Spekreijse [18].

For the sake of simplicity, Eq. (17) is conservatively discretized as Eq. (18) by the Euler forward time stepping.

$$\bar{u}^{n+1}_{i,j} = \bar{u}^n_{i,j} - \frac{\Delta t}{\Delta x}(\hat{f}^n_{i+1/2,j} - \hat{f}^n_{i-1/2,j}) - \frac{\Delta t}{\Delta y}(\hat{g}^n_{i,j+1/2} - \hat{g}^n_{i,j-1/2}). \tag{18}$$

For upwind discretization, $f(u)$ and $g(u)$ are split as

$$f(u) = f^+(u) + f^-(u), \quad g(u) = g^+(u) + g^-(u), \tag{19}$$

where

$$\frac{\mathrm{d}f^+(u)}{\mathrm{d}u} \geqslant 0, \frac{\mathrm{d}f^-(u)}{\mathrm{d}u} \leqslant 0, \quad \frac{\mathrm{d}g^+(u)}{\mathrm{d}u} \geqslant 0, \quad \frac{\mathrm{d}g^-(u)}{\mathrm{d}u} \leqslant 0 \quad \forall u \in \Re. \tag{20}$$

Then, numerical fluxes in Eq. (18) can be written as

$$\hat{f}_{i+1/2,j} = \hat{f}^+_{i+1/2,j} + \hat{f}^-_{i+1/2,j}, \quad \hat{g}_{i,j+1/2} = \hat{g}^+_{i,j+1/2} + \hat{g}^-_{i,j+1/2}. \tag{21}$$

Using these splitting, we can write numerical flux differences as

$$\begin{aligned}
\frac{\Delta t}{\Delta x}(\hat{f}^n_{i+1/2,j} - \hat{f}^n_{i-1/2,j}) &= \frac{\Delta t}{\Delta x}(\hat{f}^{n,-}_{i+1/2,j} - \hat{f}^{n,-}_{i-1/2,j}) + \frac{\Delta t}{\Delta x}(\hat{f}^{n,+}_{i+1/2,j} - \hat{f}^{n,+}_{i-1/2,j}) = -A^n_{i+1/2,j}\Delta^x_+ \bar{u}^n_{i,j} + B^n_{i-1/2,j}\Delta^x_+ \bar{u}^n_{i-1,j} \\
&= -A^n_{i+1/2,j}(\bar{u}^n_{i+1,j} - \bar{u}^n_{i,j}) + B^n_{i-1/2,j}(\bar{u}^n_{i,j} - \bar{u}^n_{i-1,j}), \\
\frac{\Delta t}{\Delta y}(\hat{g}^n_{i,j+1/2} - \hat{g}^n_{i,j-1/2}) &= \frac{\Delta t}{\Delta y}(\hat{g}^{n,-}_{i,j+1/2} - \hat{g}^{n,-}_{i,j-1/2}) + \frac{\Delta t}{\Delta y}(\hat{g}^{n,+}_{i,j+1/2} - \hat{g}^{n,+}_{i,j-1/2}) = -C^n_{i,j+1/2}\Delta^y_+ \bar{u}^n_{i,j} + D^n_{i,j-1/2}\Delta^y_+ \bar{u}^n_{i,j-1} \\
&= -C^n_{i,j+1/2}(\bar{u}^n_{i,j+1} - \bar{u}^n_{i,j}) + D^n_{i,j-1/2}(\bar{u}^n_{i,j} - \bar{u}^n_{i,j-1}),
\end{aligned}$$

where $A^n_{i+1/2,j}, \ldots, D^n_{i,j-1/2}$ are related to numerical approximation of Eq. (20) at cell-interfaces. Putting above expressions into Eq. (18), we have

$$\bar{u}^{n+1}_{i,j} = \bar{u}^n_{i,j} + A^n_{i+1/2,j}(\bar{u}^n_{i+1,j} - \bar{u}^n_{i,j}) - B^n_{i-1/2,j}(\bar{u}^n_{i,j} - \bar{u}^n_{i-1,j}) + C^n_{i,j+1/2}(\bar{u}^n_{i,j+1} - \bar{u}^n_{i,j}) - D^n_{i,j-1/2}(\bar{u}^n_{i,j} - \bar{u}^n_{i,j-1}) \tag{22}$$

or

$$\begin{aligned}
\bar{u}^{n+1}_{i,j} = {} & (1 - A^n_{i+1/2,j} - B^n_{i-1/2,j} - C^n_{i,j+1/2} - D^n_{i,j-1/2})\bar{u}^n_{i,j} + A^n_{i+1/2,j}\bar{u}^n_{i+1,j} + B^n_{i-1/2,j}\bar{u}^n_{i-1,j} + C^n_{i,j+1/2}\bar{u}^n_{i,j+1} \\
& + D^n_{i,j-1/2}\bar{u}^n_{i,j-1}.
\end{aligned} \tag{23}$$

If Eq. (23) satisfies the TVD condition, each coefficient should satisfy the following positivity conditions [1,2].

$$A^n_{i+1/2,j} \geqslant 0, \quad B^n_{i-1/2,j} \geqslant 0, \quad C^n_{i,j+1/2} \geqslant 0, \quad D^n_{i,j-1/2} \geqslant 0, \tag{24}$$

$$1 - A^n_{i+1/2,j} - B^n_{i-1/2,j} - C^n_{i,j+1/2} - D^n_{i,j-1/2} \geqslant 0. \tag{25}$$

From Eqs. (24) and (25), $\bar{u}^{n+1}_{i,j}$ is expressed as a convex combination of $\bar{u}^n_{i,j}$, $\bar{u}^n_{i\pm1,j}$ and $\bar{u}^n_{i,j\pm1}$ with positive coefficients that add up to one. Thus, the following discrete maximum principle is satisfied.

$$m_{i,j} \leqslant \bar{u}^{n+1}_{i,j} \leqslant M_{i,j}, \tag{26}$$

where

$$m_{i,j} = \min(\bar{u}^n_{i-1,j}, \bar{u}^n_{i,j-1}, \bar{u}^n_{i,j}, \bar{u}^n_{i+1,j}, \bar{u}^n_{i,j+1}),$$

$$M_{i,j} = \max(\bar{u}^n_{i-1,j}, \bar{u}^n_{i,j-1}, \bar{u}^n_{i,j}, \bar{u}^n_{i+1,j}, \bar{u}^n_{i,j+1}).$$

From Eqs. (7) and (9) and Fig. 1, MLP region is clearly contained in TVD region. Thus, Eqs. (24)–(26) are also satisfied by MLP condition. For more details, all of the coefficients, $A^n_{i+1/2,j}, \ldots, D^n_{i,j-1/2}$, can be expressed on an equidistant mesh with size h as follows:

$$\begin{aligned}
A^n_{i+1/2,j} &= -\frac{\Delta t}{h} \cdot \frac{f^-(u^{R,n}_{i+1/2,j}) - f^-(u^{R,n}_{i-1/2,j})}{u^{R,n}_{i+1/2,j} - u^{R,n}_{i-1/2,j}} \cdot \frac{u^{R,n}_{i+1/2,j} - u^{R,n}_{i-1/2,j}}{\bar{u}^n_{i+1,j} - \bar{u}^n_{i,j}}, \\
B^n_{i-1/2,j} &= +\frac{\Delta t}{h} \cdot \frac{f^+(u^{L,n}_{i+1/2,j}) - f^+(u^{L,n}_{i-1/2,j})}{u^{L,n}_{i+1/2,j} - u^{L,n}_{i-1/2,j}} \cdot \frac{u^{L,n}_{i+1/2,j} - u^{L,n}_{i-1/2,j}}{\bar{u}^n_{i,j} - \bar{u}^n_{i-1,j}}, \\
C^n_{i,j+1/2} &= -\frac{\Delta t}{h} \cdot \frac{g^-(u^{R,n}_{i,j+1/2}) - g^-(u^{R,n}_{i,j-1/2})}{u^{R,n}_{i,j+1/2} - u^{R,n}_{i,j-1/2}} \cdot \frac{u^{R,n}_{i,j+1/2} - u^{R,n}_{i,j-1/2}}{\bar{u}^n_{i,j+1} - \bar{u}^n_{i,j}}, \\
D^n_{i,j-1/2} &= +\frac{\Delta t}{h} \cdot \frac{g^+(u^{L,n}_{i,j+1/2}) - g^+(u^{L,n}_{i,j-1/2})}{u^{L,n}_{i,j+1/2} - u^{L,n}_{i,j-1/2}} \cdot \frac{u^{L,n}_{i,j+1/2} - u^{L,n}_{i,j-1/2}}{\bar{u}^n_{i,j} - \bar{u}^n_{i,j-1}},
\end{aligned} \tag{27}$$

where

$$\begin{aligned}
u^{R,n}_{i+1/2,j} &= \bar{u}^n_{i,j} + \frac{1}{2}\phi(R^n_{i,j})(\bar{u}^n_{i,j} - \bar{u}^n_{i-1,j}), \\
u^{L,n}_{i-1/2,j} &= \bar{u}^n_{i,j} - \frac{1}{2}\phi\left(\frac{1}{R^n_{i,j}}\right)(\bar{u}^n_{i+1,j} - \bar{u}^n_{i,j}), \\
u^{R,n}_{i,j+1/2} &= \bar{u}^n_{i,j} + \frac{1}{2}\phi(S^n_{i,j})(\bar{u}^n_{i,j} - \bar{u}^n_{i,j-1}), \\
u^{L,n}_{i,j-1/2} &= \bar{u}^n_{i,j} - \frac{1}{2}\phi\left(\frac{1}{S^n_{i,j}}\right)(\bar{u}^n_{i,j+1} - \bar{u}^n_{i,j}),
\end{aligned} \tag{28}$$

and

$$R^n_{i,j} = \frac{\bar{u}^n_{i+1,j} - \bar{u}^n_{i,j}}{\bar{u}^n_{i,j} - \bar{u}^n_{i-1,j}}, \quad S^n_{i,j} = \frac{\bar{u}^n_{i,j+1} - \bar{u}^n_{i,j}}{\bar{u}^n_{i,j} - \bar{u}^n_{i,j-1}}. \tag{29}$$

ϕ is a limiter function, and the region of ϕ to satisfy the maximum principle, Eq. (26), has to be determined. From Eqs. (19) and (27) and the Mean Value Theorem, positivity condition of Eq. (24) is obtained if following inequalities are satisfied.

$$\begin{aligned}
&\frac{u^{R,n}_{i+1/2,j} - u^{R,n}_{i-1/2,j}}{\bar{u}^n_{i+1,j} - \bar{u}^n_{i,j}} \geqslant 0, \quad \frac{u^{L,n}_{i+1/2,j} - u^{L,n}_{i-1/2,j}}{\bar{u}^n_{i,j} - \bar{u}^n_{i-1,j}} \geqslant 0, \\
&\frac{u^{R,n}_{i,j+1/2} - u^{R,n}_{i,j-1/2}}{\bar{u}^n_{i,j+1} - \bar{u}^n_{i,j}} \geqslant 0, \quad \frac{u^{L,n}_{i,j+1/2} - u^{L,n}_{i,j-1/2}}{\bar{u}^n_{i,j} - \bar{u}^n_{i,j-1}} \geqslant 0.
\end{aligned} \tag{30}$$

By inserting Eq. (28) into Eq. (30), Eq. (30) is satisfied if

$$1+\frac{1}{2}\phi(r)-\frac{1}{2}\phi(s)\cdot\frac{1}{s}\geqslant 0 \quad \forall r,s\in\Re. \tag{31}$$

In addition, from the uniform boundedness of the left-hand side of Eq. (30), we obtain

$$\phi(r)-\phi(s)\cdot\frac{1}{s}\leqslant 2M \quad \forall r,s\in\Re, \quad M\in(0,\infty). \tag{32}$$

By combining Eqs. (31) and (32), we have

$$-2\leqslant\phi(r)-\phi(s)\cdot\frac{1}{s}\leqslant 2M \quad \forall r,s\in\Re, \quad M\in(0,\infty). \tag{33}$$

Eq. (33) is satisfied if

$$\mu\leqslant\phi(r)\leqslant M \quad \forall r\in\Re, \tag{34}$$

and

$$-M\leqslant\frac{\phi(r)}{r}\leqslant 2+\mu \quad \forall r\in\Re. \tag{35}$$

where $\mu\in[-2,0]$.

As shown in Fig. 1, TVD limiting region given by Sweby [2] clearly satisfies Eqs. (34) and (35), and MLP limiting region clearly lies within TVD limiting region. Therefore, MLP schemes satisfy the discrete maximum principle of Eq. (26). In a similar manner, one can readily prove it for three-dimensional scalar conservation law. Thus, we have the following theorem.

Theorem 1. *When applied to multi-dimensional scalar conservation law, the fully discrete scheme using MLP limiting satisfies the following maximum principle,*

$$\bar{u}^{\min}_{\text{neighbor}}\leqslant\bar{u}^{n+1}_{i,j}\leqslant\bar{u}^{\max}_{\text{neighbor}}. \tag{36}$$

Next, let us examine the role of multi-dimensional limiting condition,

$$\bar{u}^{\min}_{\text{neighbor}}\leqslant u\leqslant\bar{u}^{\max}_{\text{neighbor}}, \tag{37}$$

in MLP scheme. Using multi-dimensional limiting condition at nth level, Barth also proved maximum principles [21], and he implemented a second- or third-order version of his scheme on unstructured meshes. MLP shares some similarities with Barth's approach in a sense that both schemes exploit benefits of multi-dimensional limiting condition. However, in derivation and implementation steps, there are several differences between Barth's limiter and MLP approach.

First of all, while quadrature points are considered in Barth's approach, only cell-vertex points are considered in MLP limiting. In case of linear reconstruction, cell-vertex point always has maximum or minimum interpolated value. Thus, if we impose multi-dimensional limiting condition on cell-vertex points, it automatically satisfies limiting cases for quadrature points. Thus, maximum principles are automatically satisfied at cell-vertex points in linear reconstruction case. For more than linear reconstruction, MLP limiting avoids quadrature points for computational efficiency. Instead, only a slope obtained by local higher-order polynomial interpolation is used.

Secondly, it appears that both Barth's and Spekreijse's approaches are similar in defining maximum or minimum cell-average values among neighboring cells. If we implement neighboring cells used in Barth's (or Spekreijse's) approach on two-dimensional structured mesh, stencil taking part in limiting cell-vertex points is five grid points, while full nine-point stencil is used in MLP limiting (see Fig. 2).

Finally, in deriving Barth's limiters [19–21], only the multi-dimensional limiting condition, Eq. (37), is extensively used. In MLP limiting, as will be shown in Lemma 1, 2 in the next Section, TVD interpolation and multi-dimensional limiting condition are actively used, and both are tightly coupled. As a result, the final limiting form of MLP contains a lot of informations provided by TVD interpolation.

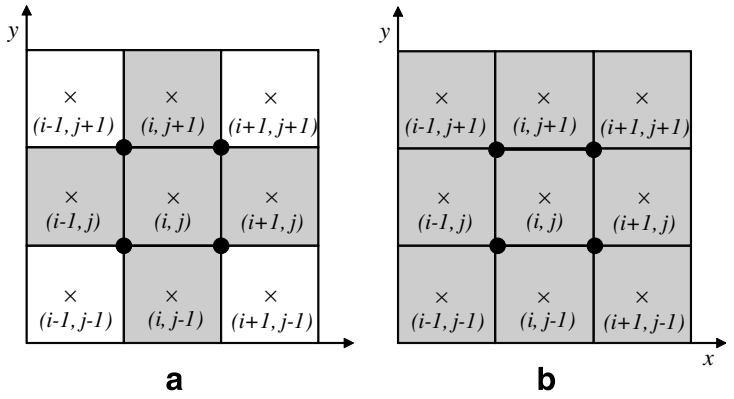

Fig. 2. Comparison of stencils for defining $\bar{u}^{\min}_{\text{neighbor}}$ or $\bar{u}^{\max}_{\text{neighbor}}$. One of the gray-colored cells is used as maximum or minimum cell-average: (a) Spekreijse's (or Barth's) concept and (b) present method (MLP approach).

2.3. Difficulties in three-dimensional extension

In two-dimensional setting, performance of MLP is quite satisfactory. Through extensive tests including shock wave/vortex interaction, shock wave/boundary layer interaction and viscous shock-tube problem, MLP turned out to be very effective in controlling oscillation for two-dimensional compressible flow [16]. However, for computational efficiency and implementation in three-dimensional application, the original formulation of MLP has to be changed.

First of all, the manner to specify $\left(\hat{q}^{\min}_{\text{neighbor}}, \hat{q}^{\max}_{\text{neighbor}}\right)$ in Eq. (8) has to be modified. In deriving the range of parameter α, $\left(\hat{q}^{\min}_{\text{neighbor}}, \hat{q}^{\max}_{\text{neighbor}}\right)$ around a vertex point was determined by checking neighboring distribution of property into four subcases according to the gradient angle θ_j. In other words, depending on the value of θ_j and the sign of property gradient $\left(\frac{\partial \hat{q}}{\partial x}, \frac{\partial \hat{q}}{\partial y}\right)$, $\left(\hat{q}^{\min}_{\text{neighbor}}, \hat{q}^{\max}_{\text{neighbor}}\right)$ was determined among neighboring cell-averaged values. For example, if $\frac{\partial \hat{q}}{\partial x} > 0$ and $\frac{\partial \hat{q}}{\partial y} > 0$, $(\hat{q}_{i+1,j+1}, \hat{q}_{i,j})$ is the maximum and minimum value around a vertex point $(i + 1/2, j + 1/2)$. Similarly, if $\frac{\partial \hat{q}}{\partial x} < 0$ and $\frac{\partial \hat{q}}{\partial y} > 0$, $(\hat{q}_{i,j+1}, \hat{q}_{i+1,j})$ would be the maximum and minimum value (see Fig. 3).

In this process, the basic assumption is that the sign of gradient around a vertex point is locally constant and the gradient direction can be uniquely determined, which is more or less reasonable in two-dimensional flow, because the number of cells around a vertex point is four and cells belong to the same plane. In three-dimensional situation, however, the sign of gradient may not be uniquely determined due to complex flow structure, such as three-dimensional interactions of shock wave, vortex and boundary layer. Moreover, there are eight cells around a vertex point, and cells do not belong to the same plane. All these facts indicate that the assumption of the locally constant gradient is incompatible with general situation. Without gradient information, however, it is not clear to explicitly define $\left(\hat{q}^{\min}_{\text{neighbor}}, \hat{q}^{\max}_{\text{neighbor}}\right)$. Fig. 4 shows an example in which the local gradient direction at $(i + 1/2, j + 1/2, k + 1/2)$ is difficult to define. This case may actually happen in three-dimensional complex shock structure. In Fig. 4, the gradient direction based on lower four cells is different from the one obtained by upper four cells. In general, to obtain $\left(\hat{q}^{\min}_{\text{neighbor}}, \hat{q}^{\max}_{\text{neighbor}}\right)$, six different subcases should be compared which is extremely cumbersome and computationally very inefficient. Thus, explicit evaluation of $\left(\hat{q}^{\min}_{\text{neighbor}}, \hat{q}^{\max}_{\text{neighbor}}\right)$ is discarded, and *max.* or *min.* function is adopted to simplify the derivation procedure. This will be shown in the next subsection.

The next thing to be modified is related to the gradient angle. In Ref. [16], the gradient angle θ was introduced to incorporate effect of discontinuity which is not aligned with local grid lines. However, once we adopt *max.* and *min.* function instead of $\left(\hat{q}^{\min}_{\text{neighbor}}, \hat{q}^{\max}_{\text{neighbor}}\right)$, the gradient angle is no longer necessary. In actual implementation, $\tilde{\theta}$ and $\bar{\theta}$ in Eq. (9) are approximated as a representative angle θ which is estimated by

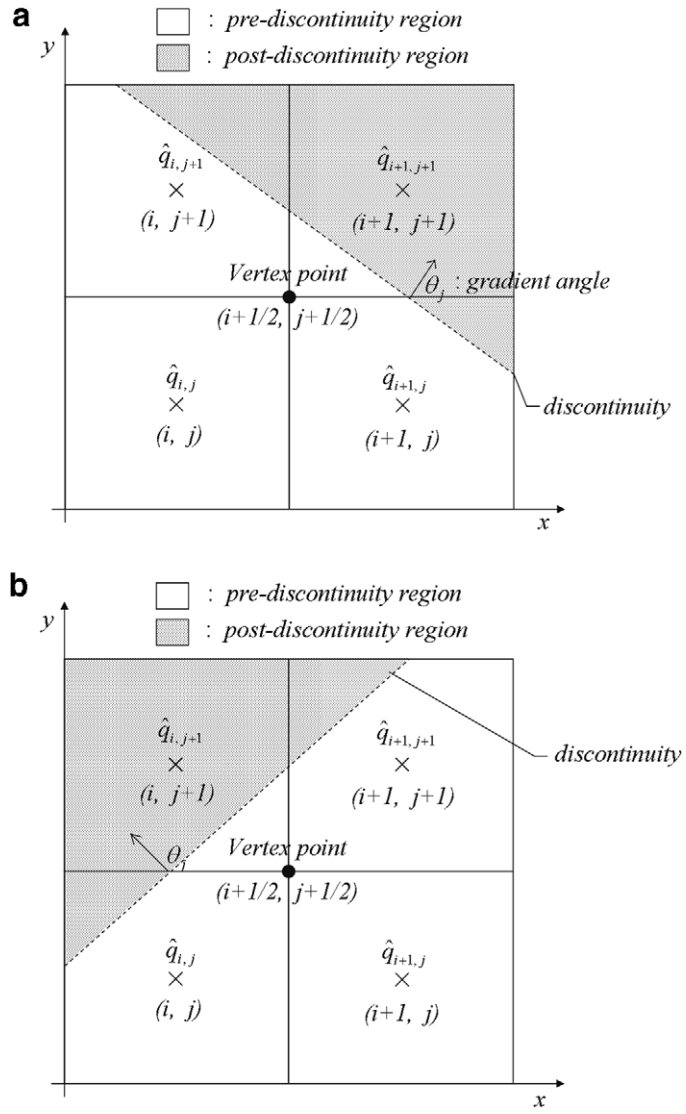

Fig. 3. Example illustrating the relation between gradient angle and cell-averaged values: (a) $0^\circ < \theta_j < 90^\circ$ corresponding to $\left(\frac{\partial \bar{q}}{\partial x} > 0, \frac{\partial \bar{q}}{\partial y} > 0\right)$ and (b) $90^\circ < \theta_j < 180^\circ$ corresponding to $\left(\frac{\partial \bar{q}}{\partial x} < 0, \frac{\partial \bar{q}}{\partial y} > 0\right)$.

$$\theta_{i,j} = \tan^{-1}\left(\frac{\hat{q}_{i+1,j} - \hat{q}_{i-1,j}}{\hat{q}_{i,j+1} - \hat{q}_{i,j-1}}\right) = \tan^{-1}\left(\frac{\Delta\hat{q}^x_{i,j}}{\Delta\hat{q}^y_{i,j}}\right). \tag{38}$$

Thus, from Eq. (9), duplicate arithmetic operation is inevitable in computing θ and $\tan\theta$. In three-dimensional flow, at least two representative angles are necessary to define local directional cosines. This would be computationally inefficient, and the formulation of α_{3D} becomes much more complicated. Thus, we directly use the variation ratio $\left(\frac{\Delta\hat{q}^x_{i,j}}{\Delta\hat{q}^y_{i,j}}, \frac{\Delta\hat{q}^x_{i,j}}{\Delta\hat{q}^z_{i,j}}\right)$.

3. A new version of MLP

Following observation in the previous subsection, MLP for two-dimensional flow is newly derived, and it is extended to three-dimensional flow.

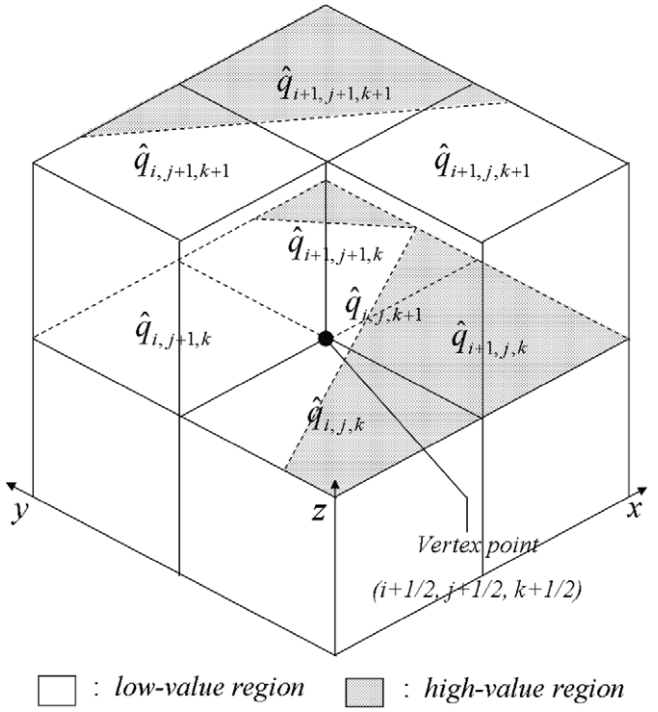

Fig. 4. Example of complex $\hat{q}$ distribution in three-dimensional flow. In this case, the assumption of locally constant gradient is not valid.

3.1. MLP for two-dimensional flow

Let us express the limiting condition of Eq. (8) more compactly as

$$\hat{q}^{\min}_{\kappa_1,\kappa_2} < q_{i+\kappa_1/2,j+\kappa_2/2} < \hat{q}^{\max}_{\kappa_1,\kappa_2}, \tag{39}$$

where $q_{i+\kappa_1/2,j+\kappa_2/2}$ is a vertex point value. $(\hat{q}^{\min}_{\kappa_1,\kappa_2}, \hat{q}^{\max}_{\kappa_1,\kappa_2})$ is the minimum and maximum cell-averaged value around the vertex point $(i+\kappa_1/2, j+\kappa_2/2)$ which is defined as

$$\hat{q}^{\min}_{\kappa_1,\kappa_2} = \min(\hat{q}_{i,j}, \hat{q}_{i+\kappa_1,j}, \hat{q}_{i,j+\kappa_2}, \hat{q}_{i+\kappa_1,j+\kappa_2}), \tag{40}$$

$$\hat{q}^{\max}_{\kappa_1,\kappa_2} = \max(\hat{q}_{i,j}, \hat{q}_{i+\kappa_1,j}, \hat{q}_{i,j+\kappa_2}, \hat{q}_{i+\kappa_1,j+\kappa_2}), \tag{41}$$

with $\kappa_1 = \pm 1$ and $\kappa_2 = \pm 1$.

By imposing the limiting condition of Eq. (39), values at four vertex points are to be estimated, and the range of the allowable variation from a cell-averaged to a cell-interface value has to be derived. Thus, it is legitimate to express the vertex point value into the sum of cell-averaged value and variation within a cell.

$$q_{i+\kappa_1/2,j+\kappa_2/2} = \hat{q}_{i,j} + \Delta q^x_{i+\kappa_1/2,j} + \Delta q^y_{i,j+\kappa_2/2}, \tag{42}$$

$$\Delta q^x_{i+\kappa_1/2,j} = q^*_{i+\kappa_1/2,j} - \hat{q}_{i,j}, \tag{43}$$

$$\Delta q^y_{i,j+\kappa_2/2} = q^*_{i,j+\kappa_2/2} - \hat{q}_{i,j}, \tag{44}$$

where $q^*_{i+\kappa_1/2,j}$ and $q^*_{i,j+\kappa_2/2}$ is temporary cell-interface value at $\left(i+\frac{\kappa_1}{2}, j\right)$ and $\left(i, j+\frac{\kappa_2}{2}\right)$, respectively.

Since $(q_{i+\kappa_1/2,j}, q_{i,j+\kappa_2/2})$ are going to be determined by the MLP, the superscript * in the above expression indicates temporary value which may differ from the final cell-interface value. At this step, the temporary value, $(q^*_{i+\kappa_1/2,j}, q^*_{i,j+\kappa_2/2})$, can be evaluated by any high-order interpolation. If the vertex point value $q_{i+\kappa_1/2,j+\kappa_2/2}$ at Eq. (42) satisfies the limiting condition of Eq. (39), the temporary value is accepted as the final cell-interface value. Otherwise, some modification has to be added to $(\Delta q^x_{i+\kappa_1/2,j}, \Delta q^y_{i,j+\kappa_2/2})$.

As mentioned in Section 2.1, MLP takes TVD approach as a basic framework. Thus, $(q^*_{i+\kappa_1/2,j}, q^*_{i,j+\kappa_2/2})$ are evaluated by employing TVD MUSCL limiting, and variation along each coordinate is given by

$$\Delta q^x_{i+\kappa_1/2,j} = \frac{\kappa_1}{2}\phi(r_x)\Delta\hat{q}_{i-1/2,j}, \tag{45}$$

$$\Delta q^y_{i,j+\kappa_2/2} = \frac{\kappa_2}{2}\phi(r_y)\Delta\hat{q}_{i,j-1/2}, \tag{46}$$

where $r_x = \frac{\Delta\hat{q}_{i+1/2,j}}{\Delta\hat{q}_{i-1/2,j}}$ and $r_y = \frac{\Delta\hat{q}_{i,j+1/2}}{\Delta\hat{q}_{i,j-1/2}}$. Inserting Eqs. (45) and (46) into Eq. (42), we obtain

$$q_{i+\kappa_1/2,j+\kappa_2/2} = \hat{q}_{i,j} + \frac{\kappa_1}{2}\phi(r_x)\Delta\hat{q}_{i-1/2,j} + \frac{\kappa_2}{2}\phi(r_y)\Delta\hat{q}_{i,j-1/2}. \tag{47}$$

The vertex point value of Eq. (47), however, does not satisfy the limiting condition of Eq. (39) at all vertex points, which necessitate the control of $(\phi(r_x), \phi(r_y))$. The form of Eq. (42) is exactly satisfied in linear distribution. For higher-order distribution, Gaussian quadrature points can be employed along a cell-interface. For the purpose of computational efficiency, however, Eq. (42) is adopted in this work.

From Eqs. (39) and (42), we have

$$\hat{q}^{\min}_{\kappa_1,\kappa_2} \leqslant \hat{q}_{i,j} + \Delta q^x_{i+\kappa_1/2,j} + \Delta q^y_{i,j+\kappa_2/2} \leqslant \hat{q}^{\max}_{\kappa_1,\kappa_2}. \tag{48}$$

Then, it satisfies the following two characteristics.

Lemma 1. *The multi-dimensional limiting condition, Eq. (48), is satisfied at all vertex points around a cell, if and only if the limiting condition is satisfied only at the maximum and minimum vertex points.*

Proof 1. Let us consider four cases according to the sign of variation.

$$\text{(a) } \Delta q^x_{i+\kappa_1/2,j} \geqslant 0 \quad \text{and} \quad \Delta q^y_{i,j+\kappa_2/2} \geqslant 0, \tag{49}$$

$$\text{(b) } \Delta q^x_{i+\kappa_1/2,j} \geqslant 0 \quad \text{and} \quad \Delta q^y_{i,j+\kappa_2/2} < 0, \tag{50}$$

$$\text{(c) } \Delta q^x_{i+\kappa_1/2,j} < 0 \quad \text{and} \quad \Delta q^y_{i,j+\kappa_2/2} \geqslant 0, \tag{51}$$

$$\text{(d) } \Delta q^x_{i+\kappa_1/2,j} < 0 \quad \text{and} \quad \Delta q^y_{i,j+\kappa_2/2} < 0. \tag{52}$$

Let us consider the case of (b). From Eq. (43), upper bound of Eq. (48) is

$$q^*_{i+\kappa_1/2,j} + \Delta q^y_{i,j+\kappa_2/2} \leqslant \hat{q}^{\max}_{\kappa_1,\kappa_2}. \tag{53}$$

Since $\Delta q^y_{i,j+\kappa_2/2}$ is negative,

$$q^*_{i+\kappa_1/2,j} + \Delta q^y_{i,j+\kappa_2/2} < q^*_{i+\kappa_1/2,j}. \tag{54}$$

And, the cell-interface value is evaluated by

$$q^*_{i+\kappa_1/2,j} = \hat{q}_{i,j} + \frac{\kappa_1}{2}\phi(r_x)\Delta\hat{q}_{i-1/2,j}. \tag{55}$$

Since the range of the limiter function ϕ is restricted by the TVD region of Eq. (5),

$$q^*_{i+\kappa_1/2,j} \leqslant \hat{q}_{i+\kappa_1,j}. \tag{56}$$

Also, from the definition of *max*. function, Eq. (41), we have

$$\hat{q}_{i+\kappa_1,j} \leqslant \hat{q}^{\max}_{\kappa_1,\kappa_2}. \tag{57}$$

Thus, from Eqs. (54), (56), and (57), upper bound of Eq. (53) is satisfied. From Eqs. (46) and (50), the lower bound of Eq. (48) can be expressed as

$$\hat{q}^{\min}_{\kappa_1,\kappa_2} \leqslant q^*_{i,j+\kappa_2/2} + \Delta q^x_{i+\kappa_1/2,j}. \tag{58}$$

Since $\Delta q^x_{i+\kappa_1/2,j}$ is positive,

$$q^*_{i,j+\kappa_2/2} \leqslant q^*_{i,j+\kappa_2/2} + \Delta q^x_{i+\kappa_1/2,j}. \tag{59}$$

Also, the cell-interface value at $(i, j+\kappa_2/2)$ evaluated by the TVD MUSCL limiting is given by

$$q^*_{i,j+\kappa_2/2} = \hat{q}_{i,j} + \frac{\kappa_2}{2}\phi(r_y)\Delta\hat{q}_{i,j-1/2}, \tag{60}$$

and the range of the limiter function ϕ is given by Eq. (5). Thus, we have

$$\hat{q}^{\min}_{\kappa_1,\kappa_2} \leqslant \hat{q}_{i,j+\kappa_2} \leqslant q^*_{i,j+\kappa_2/2}. \tag{61}$$

From Eqs. (59) and (61), lower bound of the limiting condition is also satisfied. Thus, the multi-dimensional limiting condition is automatically satisfied in case of (b).

Similarly, it can be shown that Eq. (48) is also satisfied in case of (c) if cell-interface values are determined by the TVD approach. Therefore, the multi-dimensional limiting condition is satisfied for all vertex points if it is satisfied only at the maximum and minimum vertex points. The proof for the converse is trivial. □

Regarding the maximum and minimum vertex point values, the following fact can be observed additionally.

Lemma 2. *The maximum vertex point value around a cell is always greater than the minimum cell-averaged value around the vertex point. On the contrary, the minimum vertex point value around a cell is always less than the maximum cell-averaged value around the vertex point.*

Proof 2. From the definition of min and max function shown in Eqs. (40) and (41), we have

$$\hat{q}^{\min}_{\kappa_1,\kappa_2} \leqslant \hat{q}_{i,j}, \tag{62}$$

$$\hat{q}_{i,j} \leqslant \hat{q}^{\max}_{\kappa_1,\kappa_2}. \tag{63}$$

For the case of the maximum vertex point, the sign of $(\Delta q^x_{i+\kappa_1/2,j}, \Delta q^y_{i,j+\kappa_2/2})$ in Eq. (48) is positive. Thus we have

$$\hat{q}_{i,j} < \hat{q}_{i,j} + \Delta q^x_{i+\kappa_1/2,j} + \Delta q^y_{i,j+\kappa_2/2}. \tag{64}$$

From Eqs. (62) and (64),

$$\hat{q}^{\min}_{\kappa_1,\kappa_2} < \hat{q}_{i,j} + \Delta q^x_{i+\kappa_1/2,j} + \Delta q^y_{i,j+\kappa_2/2}. \tag{65}$$

In case of the minimum vertex point, the sign of $(\Delta q^x_{i+\kappa_1/2,j}, \Delta q^y_{i,j+\kappa_2/2})$ in Eq. (48) is negative, as shown in Eq. (52). Thus, we have

$$\hat{q}_{i,j} + \Delta q^x_{i+\kappa_1/2,j} + \Delta q^y_{i,j+\kappa_2/2} < \hat{q}_{i,j}. \tag{66}$$

From Eqs. (63) and (66),

$$\hat{q}_{i,j} + \Delta q^x_{i+\kappa_1/2,j} + \Delta q^y_{i,j+\kappa_2/2} < \hat{q}^{\max}_{\kappa_1,\kappa_2}. \tag{67}$$

From Eqs. (65) and (67), the lemma is proven. □

Thanks to the Lemmas 1 and 2, we only need to check upper bound of the maximum vertex point value and lower bound of the minimum vertex point value to satisfy the multi-dimensional limiting condition.

Any vertex point value can be written as

$$q_{i+\kappa_1/2,j+\kappa_2/2} = \hat{q}_{i,j} + \left(1 + \frac{\Delta q^y_{i,j+\kappa_2/2}}{\Delta q^x_{i+\kappa_1/2,j}}\right)\Delta q^x_{i+\kappa_1/2,j}. \tag{68}$$

From Eq. (39), we have

$$\hat{q}^{\min}_{\kappa_1,\kappa_2} \leqslant \hat{q}_{i,j} + \left(1 + \frac{\Delta q^y_{i,j+\kappa_2/2}}{\Delta q^x_{i+\kappa_1/2,j}}\right)\Delta q^x_{i+\kappa_1/2,j} \leqslant \hat{q}^{\max}_{\kappa_1,\kappa_2}. \tag{69}$$

Since cases of the maximum or minimum vertex point value are considered, $\frac{\Delta q^y_{i,j+\kappa_2/2}}{\Delta q^x_{i+\kappa_1/2,j}}$ is always positive and Eq. (69) can be rearranged as

$$\frac{\hat{q}^{\min}_{\kappa_1,\kappa_2} - \hat{q}_{i,j}}{1 + r_{xy}} \leqslant \Delta q^x_{i+\kappa_1/2,j} \leqslant \frac{\hat{q}^{\max}_{\kappa_1,\kappa_2} - \hat{q}_{i,j}}{1 + r_{xy}}, \tag{70}$$

where $r_{xy} = \frac{\Delta q^y_{i,j+\kappa_2/2}}{\Delta q^x_{i+\kappa_1/2,j}}$ indicates the ratio of y-directional variation to x-directional one.

In case of $\Delta q^{x}_{i+\kappa_1/2,j} \geqslant 0$, which belongs to the maximum vertex point value, Eq. (70) can be simplified as

$$0 \leqslant \Delta q^{x}_{i+\kappa_1/2,j} \leqslant \frac{\hat{q}^{\max}_{\kappa_1,\kappa_2} - \hat{q}_{i,j}}{1 + r_{xy}} \tag{71}$$

or

$$0 \leqslant \frac{\kappa_1}{2}\phi(r_x)\Delta\hat{q}_{i-1/2,j} \leqslant \frac{\hat{q}^{\max}_{\kappa_1,\kappa_2} - \hat{q}_{i,j}}{1 + r_{xy}}. \tag{72}$$

As a proper limiter function, let us take ϕ of Eq. (7) describing MLP limiting region. Then, according to the range of r_x, Eq. (72) can be expressed as follows.

If $0 < r_x < 1$, Eq. (72) becomes

$$0 \leqslant \frac{\kappa_1\alpha}{2}\Delta\hat{q}_{i+1/2,j} \leqslant \frac{\hat{q}^{\max}_{\kappa_1,\kappa_2} - \hat{q}_{i,j}}{1 + r_{xy}}. \tag{73}$$

Thus, the range of α is

$$0 \leqslant \alpha \leqslant \frac{2\left(\hat{q}^{\max}_{\kappa_1,\kappa_2} - \hat{q}_{i,j}\right)}{\kappa_1(1 + r_{xy})\Delta\hat{q}_{i+1/2,j}}. \tag{74}$$

Also, for $r_x > 1$,

$$0 \leqslant \frac{\kappa_1\alpha}{2r_x}\Delta\hat{q}_{i+1/2,j} \leqslant \frac{\hat{q}^{\max}_{\kappa_1,\kappa_2} - \hat{q}_{i,j}}{1 + r_{xy}}, \tag{75}$$

And, the range of α becomes

$$0 \leqslant \alpha \leqslant \frac{2r_x(\hat{q}^{\max}_{\kappa_1,\kappa_2} - \hat{q}_{i,j})}{\kappa_1(1 + r_{xy})\Delta\hat{q}_{i+1/2,j}}. \tag{76}$$

By combining Eqs. (74) and (76), we have

$$0 \leqslant \alpha \leqslant \frac{2\max(1, r_x)(\hat{q}^{\max}_{\kappa_1,\kappa_2} - \hat{q}_{i,j})}{\kappa_1(1 + r_{xy})\Delta\hat{q}_{i+1/2,j}}. \tag{77}$$

Next, let us consider the case of $\Delta q^{x}_{i+\kappa_1/2,j} < 0$, which corresponds to the minimum vertex point value. Eq. (70) is then simplified as

$$\frac{\hat{q}^{\min}_{\kappa_1,\kappa_2} - \hat{q}_{i,j}}{1 + r_{xy}} \leqslant \Delta q^{x}_{i+\kappa_1/2,j} \leqslant 0 \tag{78}$$

or

$$\frac{\hat{q}^{\min}_{\kappa_1,\kappa_2} - \hat{q}_{i,j}}{1 + r_{xy}} \leqslant \frac{\kappa_1}{2}\phi(r_x)\Delta\hat{q}_{i-1/2,j} \leqslant 0. \tag{79}$$

Again, depending on the interval of r_x, the range of α in Eq. (79) can be identified as follows: If $0 < r_x < 1$,

$$\frac{\hat{q}^{\min}_{\kappa_1,\kappa_2} - \hat{q}_{i,j}}{1 + r_{xy}} \leqslant \frac{\kappa_1\alpha}{2}\Delta\hat{q}_{i+1/2,j} \leqslant 0, \tag{80}$$

$$0 \leqslant \alpha \leqslant \frac{2\left(\hat{q}^{\min}_{\kappa_1,\kappa_2} - \hat{q}_{i,j}\right)}{\kappa_1(1 + r_{xy})\Delta\hat{q}_{i+1/2,j}}. \tag{81}$$

And, if $r_x > 1$,

$$\frac{\hat{q}^{\min}_{\kappa_1,\kappa_2} - \hat{q}_{i,j}}{1 + r_{xy}} \leqslant \frac{\kappa_1 \alpha}{2 r_x} \Delta \hat{q}_{i+1/2,j} \leqslant 0, \tag{82}$$

$$0 \leqslant \alpha \leqslant \frac{2 r_x (\hat{q}^{\min}_{\kappa_1,\kappa_2} - \hat{q}_{i,j})}{\kappa_1 (1 + r_{xy}) \Delta \hat{q}_{i+1/2,j}}. \tag{83}$$

From Eqs. (81) and (83), we have

$$0 \leqslant \alpha \leqslant \frac{2 \max(1, r_x) (\hat{q}^{\min}_{\kappa_1,\kappa_2} - \hat{q}_{i,j})}{\kappa_1 (1 + r_{xy}) \Delta \hat{q}_{i+1/2,j}}. \tag{84}$$

Finally, by combining Eqs. (77) and (84), we have

$$0 \leqslant \alpha \leqslant \left| \frac{2 \max(1, r_x)}{(1 + r_{xy}) \Delta \hat{q}_{i+1/2,j}} \right| \min[|\hat{q}^{\max}_{\kappa_1,\kappa_2} - \hat{q}_{i,j}|, |\hat{q}^{\min}_{\kappa_1',\kappa_2'} - \hat{q}_{i,j}|]. \tag{85}$$

Consequently, the limiting, with α of Eq. (85) and ϕ of Eq. (7), satisfies the multi-dimensional limiting condition of Eq. (39). In actual computation, the maximum value of α is chosen to avoid excessive numerical dissipation.

$$\alpha = \left| \frac{2 \max(1, r_x)}{(1 + r_{xy}) \Delta \hat{q}_{i+1/2,j}} \right| \min[|\hat{q}^{\max}_{\kappa_1,\kappa_2} - \hat{q}_{i,j}|, |\hat{q}^{\min}_{\kappa_1',\kappa_2'} - \hat{q}_{i,j}|]. \tag{86}$$

For one-dimensional flow with $r_{xy} = 0$, α in Eq. (86) becomes two, and MLP is identical to one-dimensional TVD approach. For two-dimensional flow, however, r_{xy} takes some non-zero value depending on two-dimensional flow situation. As a result, MLP limiting region differs from one-dimensional TVD approach.

Following a similar procedure, the formulation of α in the y-direction can be obtained as Eq. (85), except that r_x, r_{xy} and $\Delta \hat{q}_{i+1/2,j}$ is replaced by r_y, r_{yx} and $\Delta \hat{q}_{i,j+1/2}$, respectively.

3.2. MLP for three-dimensional flow

The new version of MLP can be readily extended to three-dimensional case by taking a similar derivation procedure. Firstly, Eq. (39) is changed into the three-dimensional format as

$$\hat{q}^{\min}_{\kappa_1,\kappa_2,\kappa_3} < q_{i+\kappa_1/2,j+\kappa_2/2,k+\kappa_3/2} < \hat{q}^{\max}_{\kappa_1,\kappa_2,\kappa_3}, \tag{87}$$

where $q_{i+\kappa_1/2,j+\kappa_2/2,k+\kappa_3/2}$ is a vertex point value. $(\hat{q}^{\min}_{\kappa_1,\kappa_2,\kappa_3}, \hat{q}^{\max}_{\kappa_1,\kappa_2,\kappa_3})$ is the minimum and maximum cell-averaged value around the vertex point $(i + \kappa_1/2, j + \kappa_2/2, k + \kappa_3/2)$ as

$$\hat{q}^{\min}_{\kappa_1,\kappa_2,\kappa_3} = \min \begin{pmatrix} \hat{q}_{i,j,k}, \hat{q}_{i+\kappa_1,j+\kappa_2,k}, \hat{q}_{i+\kappa_1,j,k+\kappa_3}, \hat{q}_{i,j+\kappa_2,k+\kappa_3}, \\ \hat{q}_{i+\kappa_1,j,k}, \hat{q}_{i,j+\kappa_2,k}, \hat{q}_{i,j,k+\kappa_3}, \hat{q}_{i+\kappa_1,j+\kappa_2,k+\kappa_3} \end{pmatrix}, \tag{88}$$

$$\hat{q}^{\max}_{\kappa_1,\kappa_2,\kappa_3} = \max \begin{pmatrix} \hat{q}_{i,j,k}, \hat{q}_{i+\kappa_1,j+\kappa_2,k}, \hat{q}_{i+\kappa_1,j,k+\kappa_3}, \hat{q}_{i,j+\kappa_2,k+\kappa_3}, \\ \hat{q}_{i+\kappa_1,j,k}, \hat{q}_{i,j+\kappa_2,k}, \hat{q}_{i,j,k+\kappa_3}, \hat{q}_{i+\kappa_1,j+\kappa_2,k+\kappa_3} \end{pmatrix}, \tag{89}$$

where $\kappa_1 = \pm 1$, $\kappa_2 = \pm 1$ and $\kappa_3 = \pm 1$. The vertex point value is then expressed in terms of cell-averaged value and variations within a cell.

$$q_{i+\kappa_1/2,j+\kappa_2/2,k+\kappa_3/2} = \hat{q}_{i,j,k} + \Delta q^x_{i+\kappa_1/2,j,k} + \Delta q^y_{i,j+\kappa_2/2,k} + \Delta q^z_{i,j,k+\kappa_3/2}, \tag{90}$$

$$\Delta q^x_{i+\kappa_1/2,j,k} = q^*_{i+\kappa_1/2,j,k} - \hat{q}_{i,j,k}, \tag{91}$$

$$\Delta q^y_{i,j+\kappa_2/2,k} = q^*_{i,j+\kappa_2/2,k} - \hat{q}_{i,j,k}, \tag{92}$$

$$\Delta q^z_{i,j,k+\kappa_3/2} = q^*_{i,j,k+\kappa_3/2} - \hat{q}_{i,j,k}, \tag{93}$$

where $q^*_{i+\kappa_1/2,j,k}$, $q^*_{i,j+\kappa_2/2,k}$ and $q^*_{i,j,k+\kappa_3/2}$ is temporary cell-interface value at $\left(i + \frac{\kappa_1}{2}, j, k\right)$, $\left(i, j + \frac{\kappa_2}{2}, k\right)$ and $\left(i, j, k + \frac{\kappa_3}{2}\right)$, respectively.

In order to compute the x-directional cell-interface value, Eq. (90) is rearranged as follows:

$$q_{i+\kappa_1/2,j+\kappa_2/2,k+\kappa_3/2} = \hat{q}_{i,j,k} + (1 + r_{xy} + r_{xz})\Delta q^x_{i+\kappa_1/2,j,k}, \tag{94}$$

where $r_{xy} = \frac{\Delta q^y_{i,j+\kappa_2/2,k}}{\Delta q^x_{i+\kappa_1/2,j,k}}$ and $r_{xz} = \frac{\Delta q^z_{i,j,k+\kappa_3/2}}{\Delta q^x_{i+\kappa_1/2,j,k}}$. Although details of proof are not presented here, it can be shown easily that the lemma 1 and 2 in Section 3.1 is equally valid for three-dimensional flow. As a result, we only focus on cases of the maximum and minimum vertex point values.

From Eqs. (87) and (94),

$$\hat{q}^{\min}_{\kappa_1,\kappa_2,\kappa_3} \leqslant \hat{q}_{i,j,k} + (1 + r_{xy} + r_{xz})\Delta q^x_{i+\kappa_1/2,j,k} \leqslant \hat{q}^{\max}_{\kappa_1,\kappa_2,\kappa_3}. \tag{95}$$

Since r_{xy} and r_{xz} are positive, it can be rearranged for $\Delta q^x_{i+\kappa_1/2,j,k}$ as

$$\frac{\hat{q}^{\min}_{\kappa_1,\kappa_2,\kappa_3} - \hat{q}_{i,j,k}}{1 + r_{xy} + r_{xz}} \leqslant \Delta q^x_{i+\kappa_1/2,j,k} \leqslant \frac{\hat{q}^{\max}_{\kappa_1,\kappa_2,\kappa_3} - \hat{q}_{i,j,k}}{1 + r_{xy} + r_{xz}}. \tag{96}$$

In case of $\Delta q^x_{i+\kappa_1/2,j,k} > 0$, which belongs to the maximum vertex point, Eq. (96) is simplified as

$$0 \leqslant \Delta q^x_{i+\kappa_1/2,j,k} \leqslant \frac{\hat{q}^{\max}_{\kappa_1,\kappa_2,\kappa_3} - \hat{q}_{i,j,k}}{1 + r_{xy} + r_{xz}} \tag{97}$$

or

$$0 \leqslant \frac{\kappa_1}{2}\phi(r_x)\Delta\hat{q}_{i-1/2,j,k} \leqslant \frac{\hat{q}^{\max}_{\kappa_1,\kappa_2,\kappa_3} - \hat{q}_{i,j,k}}{1 + r_{xy} + r_{xz}}. \tag{98}$$

If $0 < r_x < 1$, Eq. (98) becomes

$$0 \leqslant \frac{\kappa_1\alpha}{2}\Delta\hat{q}_{i+1/2,j,k} \leqslant \frac{\hat{q}^{\max}_{\kappa_1,\kappa_2,\kappa_3} - \hat{q}_{i,j,k}}{1 + r_{xy} + r_{xz}}. \tag{99}$$

And, the range of α is

$$0 \leqslant \alpha \leqslant \frac{2(\hat{q}^{\max}_{\kappa_1,\kappa_2,\kappa_3} - \hat{q}_{i,j,k})}{\kappa_1(1 + r_{xy} + r_{xz})\Delta\hat{q}_{i+1/2,j,k}}. \tag{100}$$

For $r_x > 1$,

$$0 \leqslant \frac{\kappa_1\alpha}{2r_x}\Delta\hat{q}_{i+1/2,j,k} \leqslant \frac{\hat{q}^{\max}_{\kappa_1,\kappa_2,\kappa_3} - \hat{q}_{i,j,k}}{1 + r_{xy} + r_{xz}} \tag{101}$$

or

$$0 \leqslant \alpha \leqslant \frac{2r_x(\hat{q}^{\max}_{\kappa_1,\kappa_2,\kappa_3} - \hat{q}_{i,j,k})}{\kappa_1(1 + r_{xy} + r_{xz})\Delta\hat{q}_{i+1/2,j,k}}. \tag{102}$$

By combining Eqs. (100) and (102), the range of α for the maximum vertex point is given by

$$0 \leqslant \alpha \leqslant \frac{2\max(1, r_x)(\hat{q}^{\max}_{\kappa_1,\kappa_2,\kappa_3} - \hat{q}_{i,j,k})}{\kappa_1(1 + r_{xy} + r_{xz})\Delta\hat{q}_{i+1/2,j,k}}. \tag{103}$$

In case of the minimum vertex point with $\Delta q^x_{i+\kappa_1/2,j,k} < 0$, Eq. (96) becomes

$$\frac{\hat{q}^{\min}_{\kappa_1,\kappa_2,\kappa_3} - \hat{q}_{i,j,k}}{1 + r_{xy} + r_{xz}} \leqslant \Delta q^x_{i+\kappa_1/2,j,k} \leqslant 0 \tag{104}$$

or

$$\frac{\hat{q}^{\min}_{\kappa_1,\kappa_2,\kappa_3} - \hat{q}_{i,j,k}}{1 + r_{xy} + r_{xz}} \leqslant \frac{\kappa_1}{2}\phi(r_x)\Delta\hat{q}_{i-1/2,j,k} \leqslant 0. \tag{105}$$

If $0 < r_x < 1$,

$$0 \leqslant \alpha \leqslant \frac{2(\hat{q}^{\min}_{\kappa_1,\kappa_2,\kappa_3} - \hat{q}_{i,j,k})}{\kappa_1(1 + r_{xy} + r_{xz})\Delta\hat{q}_{i+1/2,j,k}}. \tag{106}$$

And, for $r_x > 1$,

$$0 \leqslant \alpha \leqslant \frac{2r_x\left(\hat{q}^{\min}_{\kappa_1,\kappa_2,\kappa_3} - \hat{q}_{i,j,k}\right)}{\kappa_1\left(1 + r_{xy} + r_{xz}\right)\Delta\hat{q}_{i+1/2,j,k}}. \tag{107}$$

By combining Eqs. (106) and (107), we have

$$0 \leqslant \alpha \leqslant \frac{2\max(1, r_x)(\hat{q}^{\min}_{\kappa_1,\kappa_2,\kappa_3} - \hat{q}_{i,j,k})}{\kappa_1(1 + r_{xy} + r_{xz})\Delta\hat{q}_{i+1/2,j,k}}. \tag{108}$$

Finally, from Eqs. (103) and (108), the range of α satisfying the three-dimensional limiting condition is given by

$$0 \leqslant \alpha \leqslant \left|\frac{2\max(1, r_x)}{(1 + r_{xy} + r_{xz})\Delta\hat{q}_{i+1/2,j,k}}\right| \min\left[|\hat{q}^{\max}_{\kappa_1,\kappa_2,\kappa_3} - \hat{q}_{i,j,k}|, |\hat{q}^{\min}_{\kappa_1',\kappa_2',\kappa_3'} - \hat{q}_{i,j,k}|\right]. \tag{109}$$

And the choice of α for the three-dimensional limiting is

$$\alpha = \left|\frac{2\max(1, r_x)}{(1 + r_{xy} + r_{xz})\Delta\hat{q}_{i+1/2,j,k}}\right| \min\left[|\hat{q}^{\max}_{\kappa_1,\kappa_2,\kappa_3} - \hat{q}_{i,j,k}|, |\hat{q}^{\min}_{\kappa_1',\kappa_2',\kappa_3'} - \hat{q}_{i,j,k}|\right]. \tag{110}$$

The formulation of α in the y- or z-direction can be similarly obtained.

3.3. General procedure of MLP for three-dimensional compressible flow

Within the framework of finite volume method, the procedure to implement MLP for three-dimensional compressible flow is explained. The x-directional inviscid flux vector of the three-dimensional Euler or Navier–Stokes equations in a conservative form is denoted by $\mathbf{E}$.

$$\mathbf{E}_{i+1/2,j,k} = \mathbf{E}_{i+1/2,j,k}(\mathbf{Q}^{\mathrm{L}}_{i+1/2,j,k}, \mathbf{Q}^{\mathrm{R}}_{i+1/2,j,k}), \tag{111}$$

where $\mathbf{Q}$ is conservative variable vector and cell-interface value is computed directly by the MLP scheme. The choice of interpolation variable is optional in MLP schemes. It has been reported that higher-order interpolation based on characteristic decomposition yields smoother (or less oscillatory) results than conservative- or primitive-based interpolation [23]. For computational efficiency and three-dimensional application, however, primitive variables are used in the present work, and MLP limiting based on primitive variables does not induce spurious oscillations. Cell-interface value of q is determined by the MLP scheme as follows.

$$q^{\mathrm{L}}_{i+1/2,j,k} = \hat{q}_{i,j,k} + \frac{1}{2}\phi^{\mathrm{L}}_{i,j,k}\Delta\hat{q}_{i-1/2,j,k}, \tag{112}$$

$$q^{\mathrm{R}}_{i+1/2,j,k} = \hat{q}_{i+1,j,k} - \frac{1}{2}\phi^{\mathrm{R}}_{i+1,j,k}\Delta\hat{q}_{i+3/2,j,k}. \tag{113}$$

MLP limiter functions $\phi^{\mathrm{L}}_{i,j,k}$ and $\phi^{\mathrm{R}}_{i+1,j,k}$ can be expressed by

$$\phi^{\mathrm{L}}_{i,j,k} = \phi^{\mathrm{L}}(r+_x, \alpha^{\mathrm{L}}_x, \beta^{\mathrm{L}}_x) = \max(0, \min(\alpha^{\mathrm{L}}_x r^{\mathrm{L}}_x, \alpha^{\mathrm{L}}_x, \beta^{\mathrm{L}}_x)), \tag{114}$$

$$\phi^{\mathrm{R}}_{i+1,j,k} = \phi^{\mathrm{R}}(r^{\mathrm{R}}_x, \alpha^{\mathrm{R}}_x, \beta^{\mathrm{R}}_x) = \max(0, \min(\alpha^{\mathrm{R}}_x r^{\mathrm{R}}_x, \alpha^{\mathrm{R}}_x, \beta^{\mathrm{R}}_x)), \tag{115}$$

where $\alpha_x^{\mathrm{L}} = [\alpha_x]_{i,j,k}$, $\alpha_x^{\mathrm{R}} = [\alpha_x]_{i+1,j,k}$, $r_x^{\mathrm{L}} = [r_x]_{i,j,k}$ and $r_x^{\mathrm{R}} = 1/[r_x]_{i+1,j,k}$. And $[\alpha_x]_{i,j,k}$ is expressed by

$$[\alpha_x]_{i,j,k} = \left| \frac{2\max(1, [r_x]_{i,j,k})}{(1 + [r_{xy}]_{i,j,k} + [r_{xz}]_{i,j,k})\Delta\hat{q}_{i+1/2,j,k}} \right| \Gamma_{i,j,k}, \tag{116}$$

$$\Gamma_{i,j,k} = \min[|[\hat{q}^{\max}_{\kappa_1,\kappa_2,\kappa_3}]_{i,j,k} - \hat{q}_{i,j,k}|, |[\hat{q}^{\min}_{\kappa_1',\kappa_2',\kappa_3'}]_{i,j,k} - \hat{q}_{i,j,k}|], \tag{117}$$

with $[r_x]_{i,j,k} = \frac{\Delta\hat{q}_{i+1/2,j,k}}{\Delta\hat{q}_{i-1/2,j,k}}$. Also, $[r_{xy}]_{i,j,k}$ and $[r_{xz}]_{i,j,k}$ are given by

$$[r_{xy}]_{i,j,k} = \frac{\Delta q^y_{i,j+\kappa_2/2,k}}{\Delta q^x_{i+\kappa_1/2,j,k}}, \quad [r_{xz}]_{i,j,k} = \frac{\Delta q^z_{i,j,k+\kappa_3/2}}{\Delta q^x_{i+\kappa_1/2,j,k}}.$$

For the purpose of computational efficiency, $[r_{xy}]_{i,j,k}$ and $[r_{xz}]_{i,j,k}$ can be approximated as follows without compromising numerical accuracy.

$$[r_{xy}]_{i,j,k} \approx \left| \frac{\hat{q}_{i,j+1,k} - \hat{q}_{i,j-1,k}}{\hat{q}_{i+1,j,k} - \hat{q}_{i-1,j,k}} \right|, \quad [r_{xz}]_{i,j,k} \approx \left| \frac{\hat{q}_{i,j,k+1} - \hat{q}_{i,j,k-1}}{\hat{q}_{i+1,j,k} - \hat{q}_{i-1,j,k}} \right|.$$

Finally, parameters β_x^{L} and β_x^{R}, obtained from the third-order and fifth-order interpolation, are expressed as follows:

MLP with the third order interpolation (MLP3):

$$\beta_x^{\mathrm{L}} = \frac{1 + 2[r_x]_{i,j,k}}{3}, \quad \beta_x^{\mathrm{R}} = \frac{1 + 2/[r_x]_{i+1,j,k}}{3}.$$

MLP with the fifth-order interpolation (MLP5):

$$\beta_x^{\mathrm{L}} = \frac{-2/[r_x]_{i-1,j,k} + 11 + 24[r_x]_{i,j,k} - 3[r_x]_{i,j,k}[r_x]_{i+1,j,k}}{30},$$

$$\beta_x^{\mathrm{R}} = \frac{-2[r_x]_{i+3,j,k} + 11 + 24/[r_x]_{i+2,j,k} - 3/([r_x]_{i+2,j,k}[r_x]_{i+1,j,k})}{30}.$$

Numerical fluxes in the y- or z-direction can be similarly obtained.

4. Numerical results

Performance of MLP is examined through various test cases. For two-dimensional compressible flows, we perform forward facing step, double Mach reflection and isentropic vortex advection problems. Three-dimensional examples include stationary contact discontinuity, inclined normal shock discontinuity, pure vortex flow (passive vortex simulation) and oblique Lax's shock-tube problem. Moreover, three-dimensional inviscid supersonic corner flow and three-dimensional viscous shock-tube problem are also tested to examine more complex flow fields. For each numerical test, we compare accuracy and convergence characteristics of MLP with those of well-known TVD MUSCL limiters. Since MLP limiting is independent of numerical flux, Lax–Friedrichs flux splitting, Roe-type schemes [24,25] and AUSM-type schemes [26,27] are also tested as numerical fluxes. As a time integration method, LU-SGS [28] is used for steady-state flows, and the third-order TVD Runge–Kutta method [4] is used for unsteady calculation.

4.1. A Mach 3 wind tunnel with a step

Firstly, we test a Mach 3 wind tunnel with a step problem [29]. Although convectional TVD MUSCL limiters may work well, present method might have some advantage in resolving slip lines. The set up of the problem is as follows: computational domain is $0 \leqslant x \leqslant 3$ and $0 \leqslant y \leqslant 1$ with equally spaced grid points. Step height is 0.2 length units, and is located at $x = 0.6$ from the left-hand end of the tunnel. Reflective boundary conditions are applied along walls of the tunnel, and in-flow and out-flow boundary conditions are applied at the entrance (left-hand end) and the exit (right-hand end). For treatment of the singularity at corner of the step, we adopt the same technique used in [29].

In Fig. 5, we compare numerical schlieren of conventional TVD limiter (van Leer limiter) and present method (MLP5) with 240×80 and 480×160 grid points. Both van Leer limiter and MLP5 work well, but resolution of slip lines (which are often called "flag-waving" instability) is noticeably different. MLP5 captures "flag-waving" instability more clearly, while van Leer limiter mitigates it due to excessive dissipation.

4.2. Double mach reflection

The second test case is the double Mach reflection problem, which is also a very popular test case for high-resolution schemes [29]. The whole computational domain is $0 \leqslant x \leqslant 4$ and $0 \leqslant y \leqslant 1$ with equally spaced grid points. Solid wall is located at the bottom of computational domain starting from $x = 1/6$. Initially, a right-moving shock with M=10 is positioned at $(x = 1/6, y = 0)$, inclined at a 60° angle with respect to the x-axis. Reflective boundary condition is applied along the bottom wall, and computation was carried out till $t = 0.2$. See Ref. [1] for detailed description.

Fig. 6 shows density contours of conventional TVD MUSCL limiter (van Leer limiter) and present method (MLP5) with 480×120 and 1920×480 grid points. Similar to the forward facing step problem, both van Leer limiter and MLP5 give monotone solutions. In Fig. 7, we display a close-up view around the shock triple point

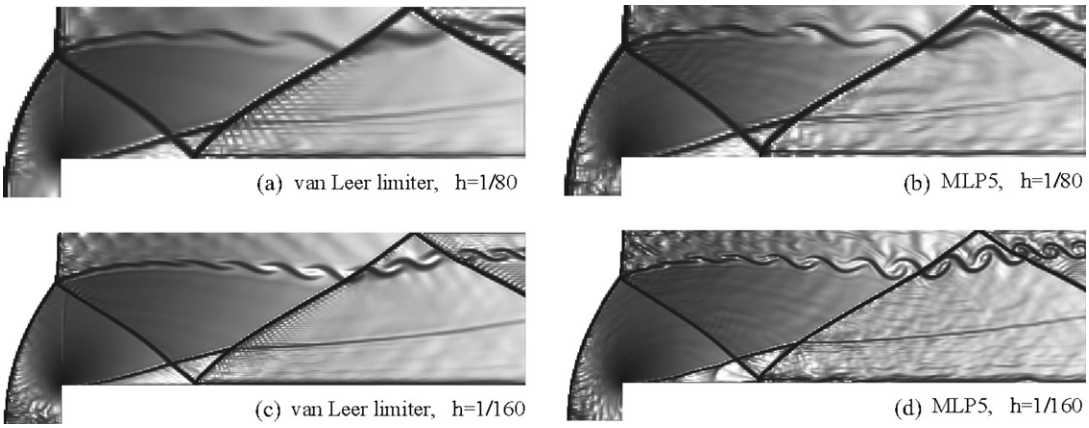

Fig. 5. Numerical schlieren of a Mach 3 wind tunnel with a step problem. Conventional TVD MUSCL limiter (van Leer limiter) and present method (MLP5) are compared with 240×80 and 480×160 grid points.

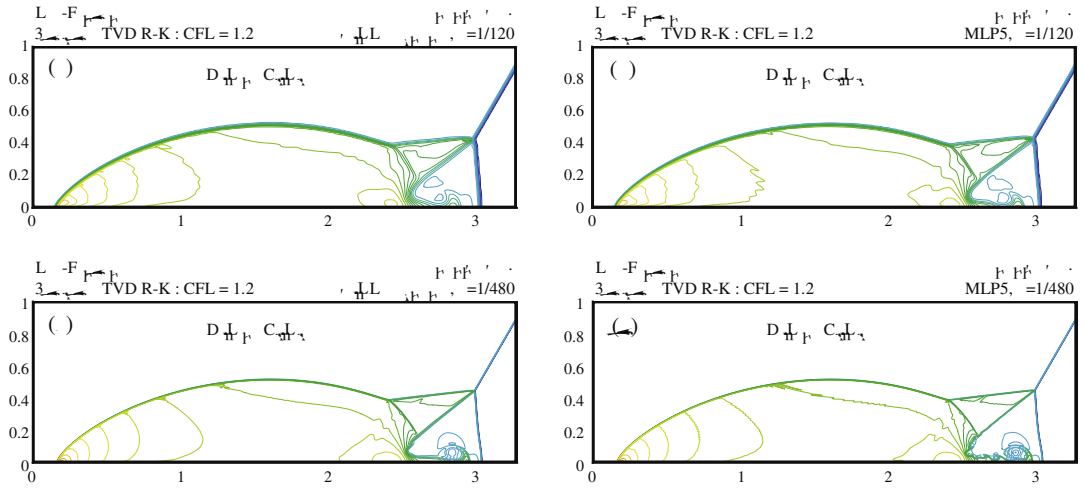

Fig. 6. Comparison of density contours for double Mach reflection problem. Thirty equally spaced contour lines from $\rho = 1.5$ to $\rho = 23.5$.

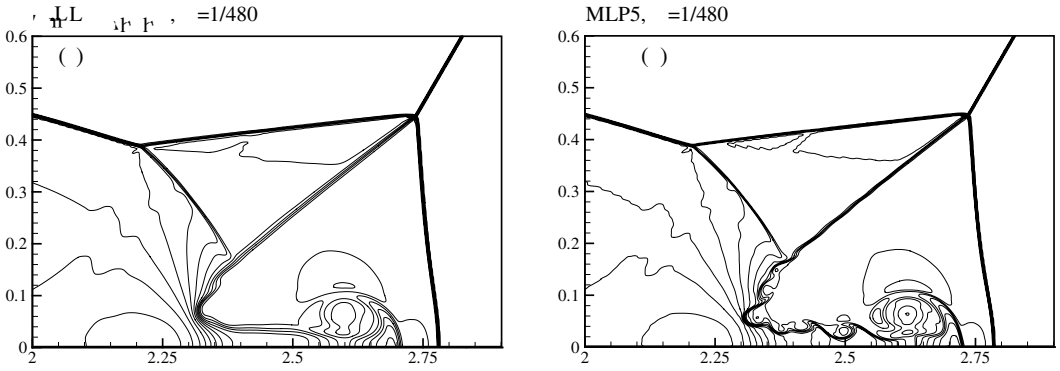

Fig. 7. Blown-up region around the double Mach stems: (a) van Leer limiter with $h = \frac{1}{480}$ and (b) MLP5 with $h = \frac{1}{480}$.

in order to examine resolution of the shear layer originated from the triple point. We can clearly see that MLP5 yields a much better performance in resolving details of the complicated flow structure.

4.3. Isentropic vortex advection

An isentropic vortex advection problem [9,12] is considered to assess multi-dimensional accuracy of MLP schemes. An isentropic vortex moving with inviscid free stream is known to provide a good test bed to validate

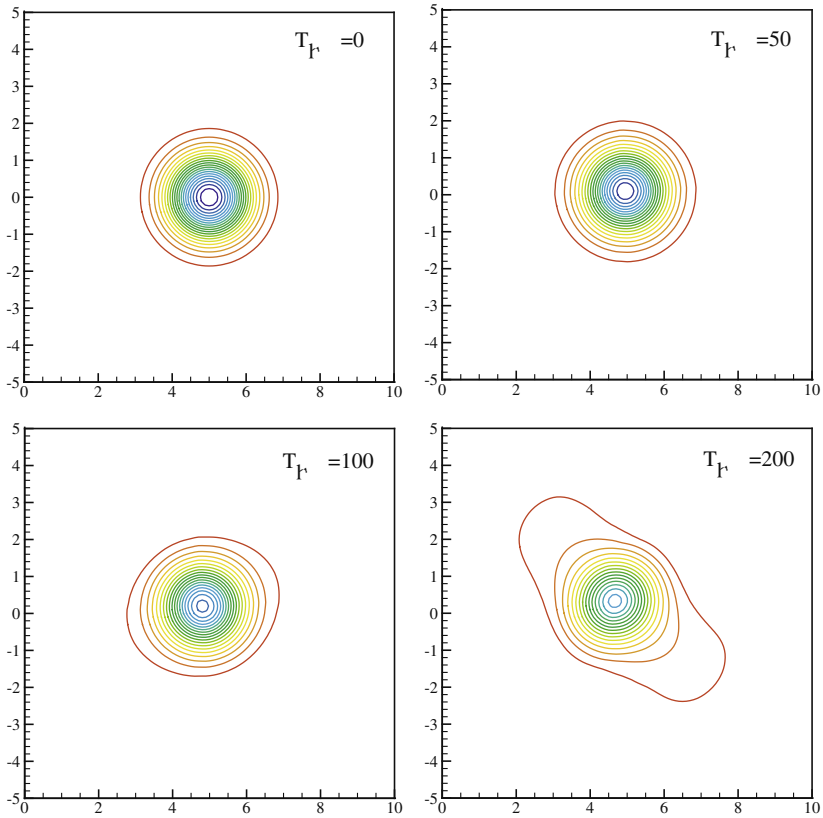

Fig. 8. Density contours of the convecting vortex at $t = 0$, 50, 100 and 200 using convectional TVD MUSCL limiter (van Leer limiter) with a 100×100 grid system: 20 equally spaced contour lines from $\rho = 0.52$ to $\rho = 0.98$.

whether a scheme can give a low-dissipative smooth solution for long-time integration. Since the flowfield is inviscid, the exact solution is just a passive advection of the initial vortex with mean velocity.

As an initial condition, an isentropic vortex is superposed to the mean flow field. Initial mean flow and perturbation values for the isentropic vortex are given by

$$u_\infty = 1, \quad v_\infty = 1, \quad p_\infty = \rho_\infty = T_\infty = 1, \quad (\delta u, \delta v) = \frac{\beta}{2\pi} e^{(1-r^2)/2}(-\bar{y}, \bar{x}), \quad \delta T = -\frac{(\gamma-1)\beta^2}{8\gamma\pi} e^{1-r^2}.$$

The vortex intensity, β, is set to 5 and $\gamma = 1.4$. Note that the vortex intensity should not be confused with β in MLP. Here, $(\bar{x}, \bar{y}) = (x - x_{v0}, y - y_{v0})$, and (x_{v0}, y_{v0}) are coordinates of the center of initial vortex: $(x_{v0}, y_{v0}) = (5, 0)$, and $r^2 = \bar{x}^2 + \bar{y}^2$. For a perfect isentropic gas, the entire flowfield is $p/\rho^\gamma = 1$.

From $\rho = \rho_\infty + \delta\rho$, $u = u_\infty + \delta u$, $v = v_\infty + \delta v$, $T = T_\infty + \delta T$, and the isentropic relation, conservative variables for the exact solution are given by

$$\rho = T^{1/(\gamma-1)} = (T_\infty + \delta T)^{1/(\gamma-1)} = \left[1 - \frac{(\gamma-1)\beta^2}{8\gamma\pi} e^{1-r^2}\right]^{1/(\gamma-1)}, \quad \rho u = \rho(u_\infty + \delta u) = \rho\left[1 - \frac{\beta}{2\pi} e^{(1-r^2)/2}\bar{y}\right],$$

$$\rho v = \rho(v_\infty + \delta v) = \rho\left[1 + \frac{\beta}{2\pi} e^{(1-r^2)/2}\bar{x}\right], \quad p = \rho^\gamma, \quad \rho e_t = \frac{p}{(\gamma-1)} + \frac{1}{2}\rho(u^2 + v^2).$$

Computational domain is set to $0 \leqslant x \leqslant 10$ and $-5 \leqslant y \leqslant 5$. Periodic boundary condition is typically used for this test. Thus, the vortex moves in the right-up direction with the free stream, and returns back to the initial location at every non-dimensional time interval $\Delta t = 10$.

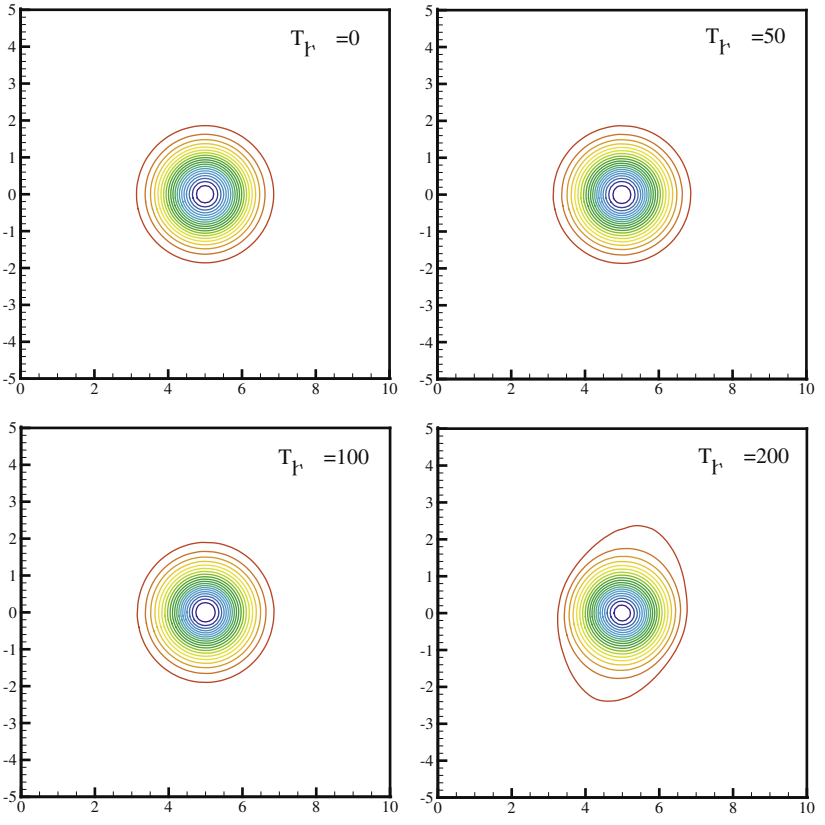

Fig. 9. Density contours of the convecting vortex at $t = 0$, 50, 100 and 200 using present method (MLP5) with a 100×100 grid system: 20 equally spaced contour lines from $\rho = 0.52$ to $\rho = 0.98$.

First of all, low-dissipative characteristic of each scheme can be found by comparing vortex shape or density profile along the center line ($y = 0$) with initial data. Figs. 8 and 9 show density contours using conventional TVD MUSCL limiter (van Leer limiter) and present method (MLP5). The grid system is a 100×100 with uniform grid size. Roe's FDS is used as a numerical flux function, and fourth order Runge–Kutta method with $\Delta t = 0.02$ is used as a time integration method. As seen in Fig. 8, vortex profile with TVD MUSCL limiter (van Leer limiter) begins to smear after $t = 100$, and what is worse, the location of vortex center does not match the exact solution due to excessive numerical dissipation. On the other hand, as in Fig. 9, present method (MLP5) can keep vortex center as well as vortex shape.

Fig. 10 shows comparison of density distribution along the vortex center line ($y = 0$). While vortex is severely smeared in case of conventional TVD limiter, present method (MLP5) keeps density distribution almost the same as the initial profile. It is also noticeable that MLP5 gives a better vortex core than the third-order polynomial without limiting.

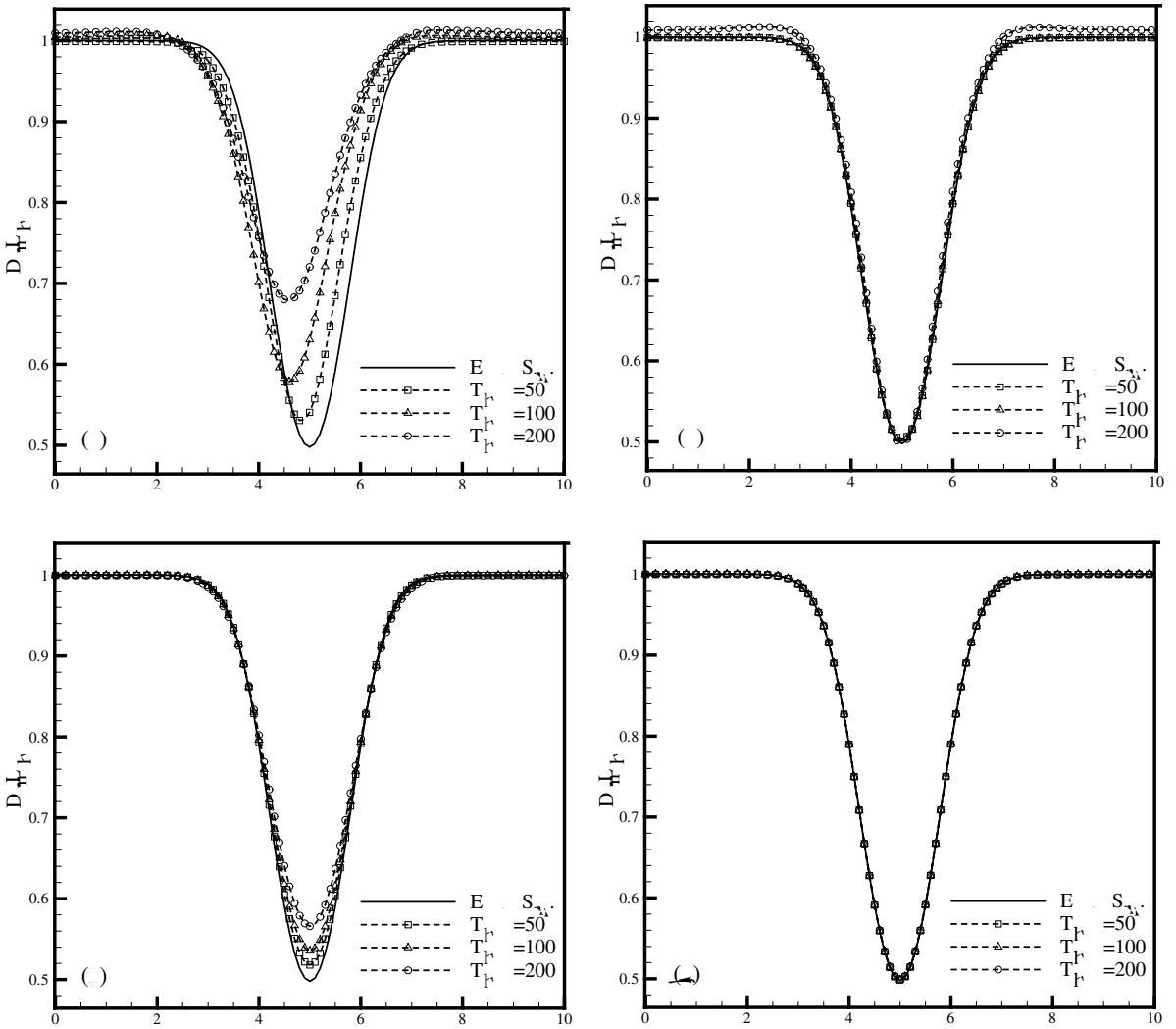

Fig. 10. Density distributions of the convecting vortex along the center line at $t = 50$, 100 and 200 with a 100×100 grid system: (a) convectional TVD MUSCL limiter (van Leer limiter), (b) present method (MLP5), (c) third order interpolation without limiting and quadrature points integration and (d) fifth order interpolation without limiting and quadrature points integration.

A grid refinement study is carried out with various grid sizes: 50×50, 100×100, 150×150 and 200×200. Table 1 shows L_1 and L_∞ error at $t = 10$. Even though present method just uses a local slope (β of Eq. (14) in Section 2.1) and does not employ Gaussian quadrature, the formal order of accuracy is clearly better than second order. L_1 and L_∞ errors of present method are much less than those of conventional TVD limiter (van leer limiter). Especially, L_1 and L_∞ errors of MLP5 with 100×100 grid are less than those of van Leer limiter with 200×200 grid. In addition, MLP5 is very competitive with the third-order polynomial interpolation without limiting.

4.4. Stationary contact discontinuity

Three-dimensional stationary contact discontinuity which is not aligned with local grid lines is considered. It is well-known that accurate capturing of contact discontinuity is closely related to accurate resolution of boundary layer and separated flow. Initial conditions are:

$$(\rho, u, v, w, p)_{\mathrm{L}} = (2.0, -0.2, 0.1, 0.1, 0.714),$$
$$(\rho, u, v, w, p)_{\mathrm{R}} = (1.0, -0.2, 0.1, 0.1, 0.714).$$

Grid system is $(20 \times 20 \times 20)$, and the contact discontinuity is inclined by 45° angle with respect to grid lines as shown in Fig. 11. All the boundary values are fixed as initial conditions.

Fig. 11 shows density distributions of six cases in which resolution of contact discontinuity is a little bit different. Result of minmod and superbee limiter is most and least diffusive, respectively. Other results look somewhat similar. For quantitative comparison, density distribution along the x-direction ($y = \text{const.}, z = \text{const.}$) is compared in Fig. 12. MLP-combined methods seem to provide similar results indicating that they are less sensitive to evaluation of β in Eq. (14).

In this test case, performance of MLP-combined methods are not so impressive, especially compared with result of superbee limiter. As will be seen in other test cases, however, over-compressive nature of superbee limiter tends to violate the entropy condition which yields unphysical results [16]. In addition, the main role of MLP is to control numerical oscillation without compromising solution accuracy in multiple dimensions.

Table 1
Grid refinement study for isentropic vortex evolution problem

Scheme	Size	L_1 error	L_1 order	L_∞ error	L_∞ order
van Leer limiter	50×50	4.6165E−03	–	8.9412E−02	–
	100×100	1.0489E−03	2.14	2.2579E−02	1.99
	150×150	4.5167E−04	2.08	1.0169E−02	1.97
	200×200	2.5121E−04	2.04	5.6879E−03	2.02
MLP-van Leer limiter	50×50	3.7699E−03	–	8.0859E−02	–
	100×100	7.1064E−04	2.41	2.0432E−02	1.98
	150×150	2.9575E−04	2.16	9.2804E−03	1.95
	200×200	1.5657E−04	2.21	5.1476E−03	2.05
MLP3	50×50	2.0713E−03	–	3.9473E−02	–
	100×100	2.9620E−04	2.81	7.2746E−03	2.44
	150×150	9.8557E−05	2.71	2.9668E−03	2.21
	200×200	4.3257E−05	2.86	1.4262E−03	2.55
MLP5	50×50	1.1441E−03	–	2.4834E−02	–
	100×100	2.2427E−04	2.35	5.5389E−03	2.16
	150×150	7.6479E−05	2.65	1.9767E−03	2.54
	200×200	4.0756E−05	2.19	1.0291E−03	2.27
Third order polynomial	50×50	1.5736E−03	–	4.1150E−02	–
	100×100	2.6245E−04	2.58	6.3480E−03	2.70
	150×150	9.6728E−05	2.46	2.0090E−03	2.84
	200×200	4.9086E−05	2.36	8.9188E−04	2.82

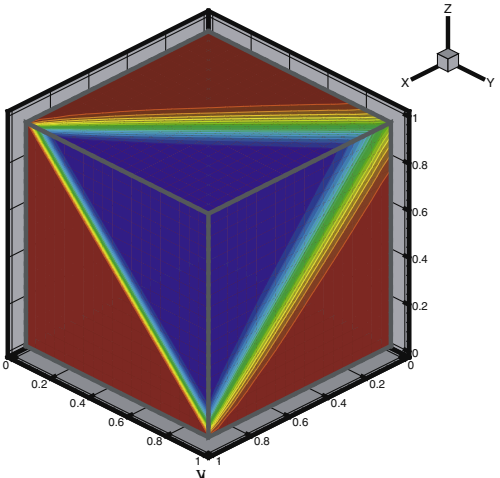

. R۲ FDS

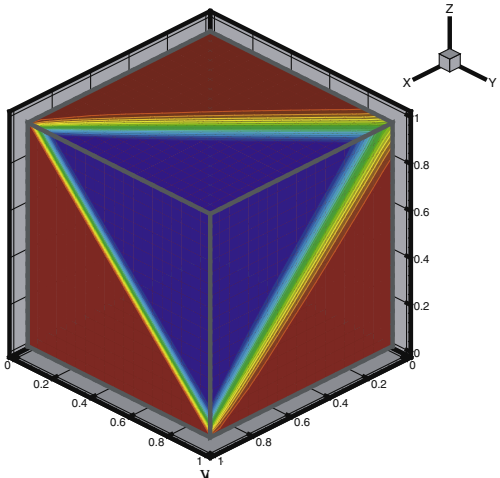

. R۲ FDS

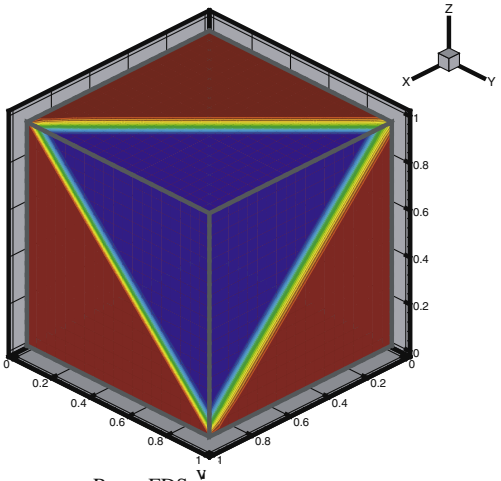

. R۲ FDS

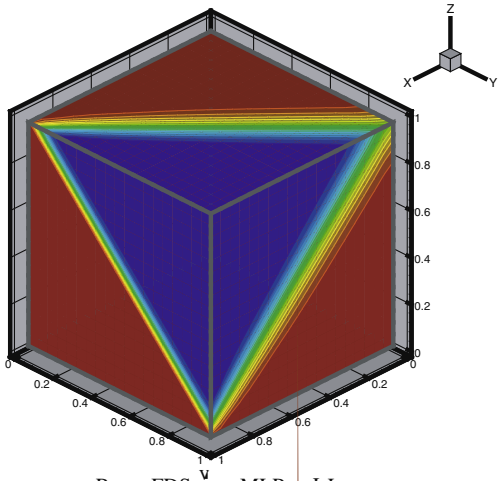

. R۲ FDS MLP-

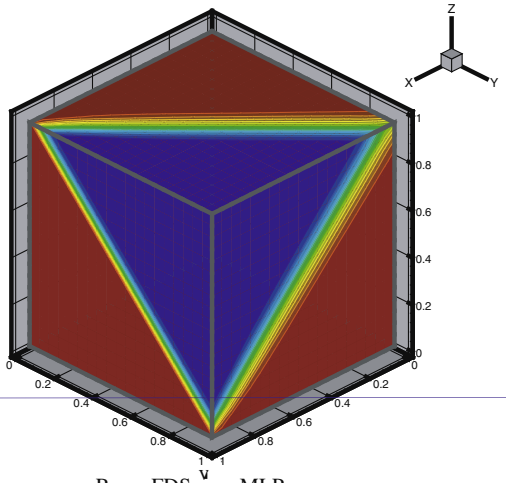

. R۲ FDS MLP-

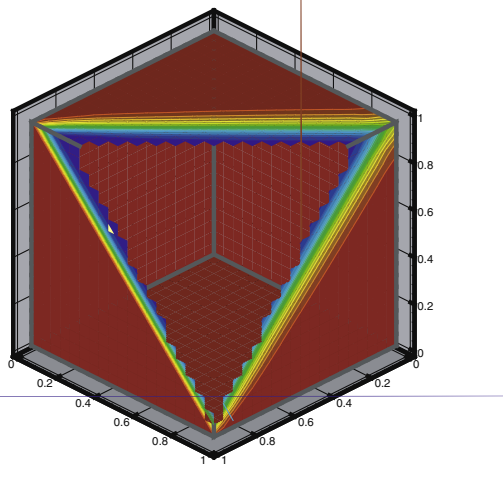

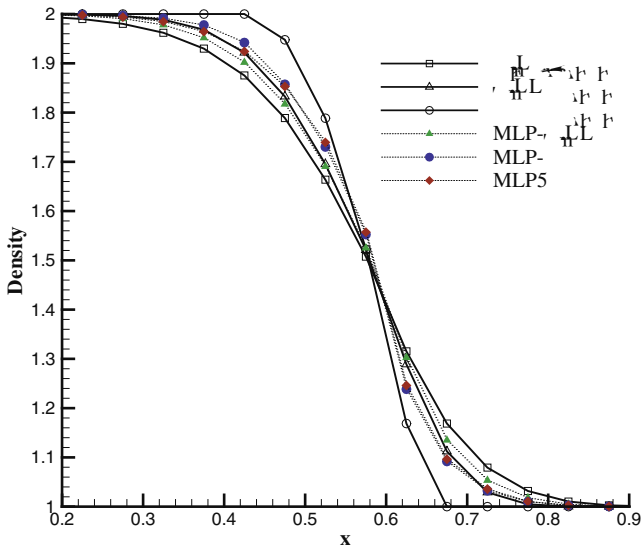

Fig. 12. Density distribution of stationary contact discontinuity by six limiting methods (x-direction). $y = z = 0.725$.

Results of Fig. 12 support that the oscillation control mechanism of MLP has not originated from excessive numerical dissipation.

4.5. Normal shock discontinuity

Similar to the previous test case, shock-capturing characteristics of MLP schemes are examined by computing a normal shock discontinuity which is not aligned with local grid lines. The free stream Mach number is five, and the normal shock discontinuity is inclined by 45° angle to each cell-surface as shown in Fig. 13. From the one-dimensional normal shock relation, the physical quantities in the post-shock region are obtained and used as initial conditions.

$$(\rho, u, v, w, p)_{\mathrm{L}} = (1.0, 2.887, 2.887, 2.887, 0.714),$$
$$(\rho, u, v, w, p)_{\mathrm{R}} = (5.0, 0.577, 0.577, 0.577, 20.71),$$

where subscript L and R indicate pre- and post-shock region, respectively. Grid system is $(20 \times 20 \times 20)$, and all boundary values are fixed as initial conditions.

Fig. 13 shows pressure contours of six different cases. As seen in Fig. 13b, visible oscillations can be observed in case of van Leer limiter, and it becomes much worse in case of superbee limiter (Fig. 13c). Fig. 14 shows convergence history of each method. Even if this test is relatively simple, results obtained by conventional limiters do not converge at all due to oscillatory behavior across the normal shock discontinuity. As in Figs. 13 and 14, MLP version conventional limiters and MLP5 provide smooth pressure contours in the post-shock region, and exhibit good convergence characteristics.

For more quantitative comparison, pressure distribution along the x-direction ($y = \text{const.}, z = \text{const.}$) are compared in Fig. 15. Conventional limiters produce some oscillatory behavior, while MLP version limiters and MLP5 maintain a monotonic shock profile. Among conventional limiters, only minmod limiter does not produce oscillation at the expense of excessive numerical dissipation.

4.6. Three-dimensional pure vortex flow (passive vortex simulation)

Vortex flow is a purely multi-dimensional phenomenon, characterized by negative pressure gradient toward vortex core and curved flow contours. Thus, flow-aligned grid system is virtually impossible, and computed

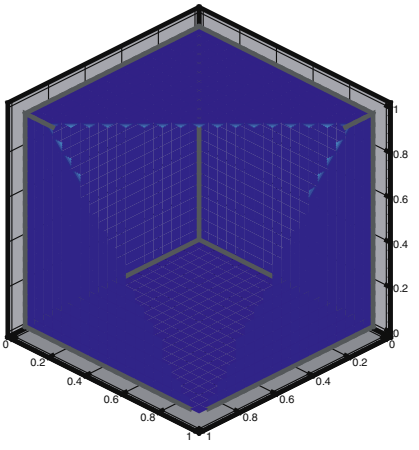

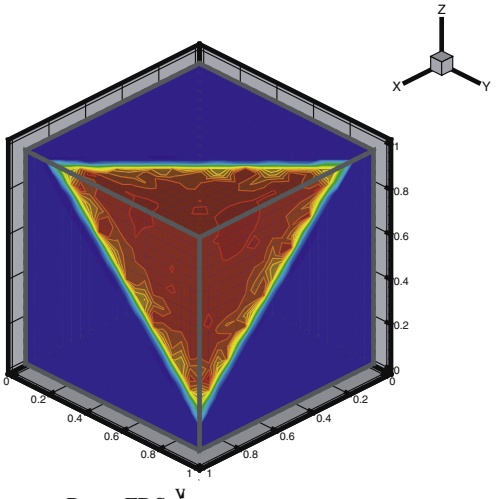

. R۲ FDS ۷ ۲ ۲۲ ۲

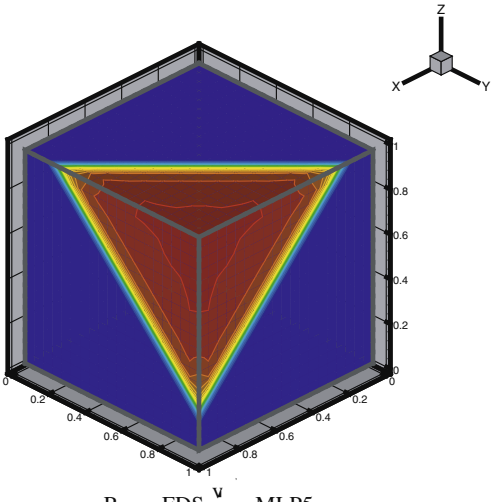

. R۲ FDS ۷ ۲ MLP5

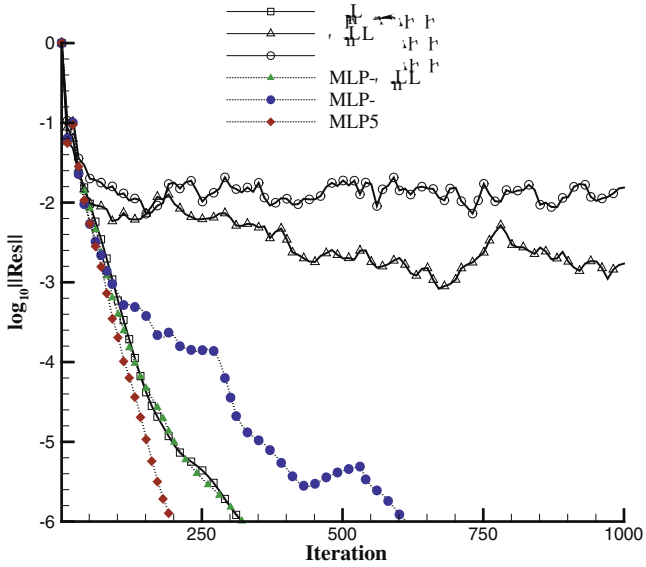

Fig. 14. Convergence history of six limiting methods for normal shock discontinuity inclined to cell-surface by 45°. CFL number is 5.0 and LU-SGS is used for time integration.

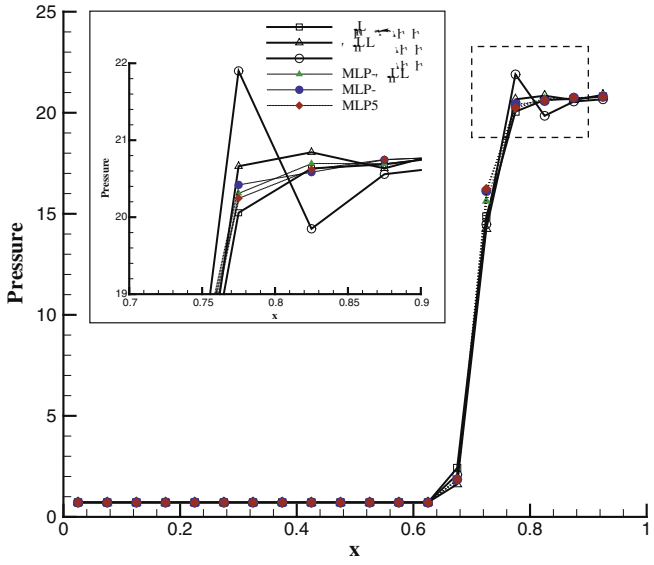

Fig. 15. Pressure distribution of six limiting methods for normal shock discontinuity inclined to cell-surface by 45° (x-direction). $y = z = 0.725$.

results are sensitive to the choice of interpolation scheme, limiting strategy and numerical fluxes. Moreover, regarding flow analysis over helicopter rotor blades, accurate prediction of vortex flow is particularly important. Accurate capturing of tip vortex released from rotor blades is directly related to performance coefficient, such as rotor thrust coefficient or blade vortex interaction (BVI). After a tip vortex element is released from a rotor blade, it remains in place and decays naturally as the blade moves away. Without including viscosity, this passive vortex simulation may evaluate critically the performance of numerical dissipation in multi-dimensional continuous region.

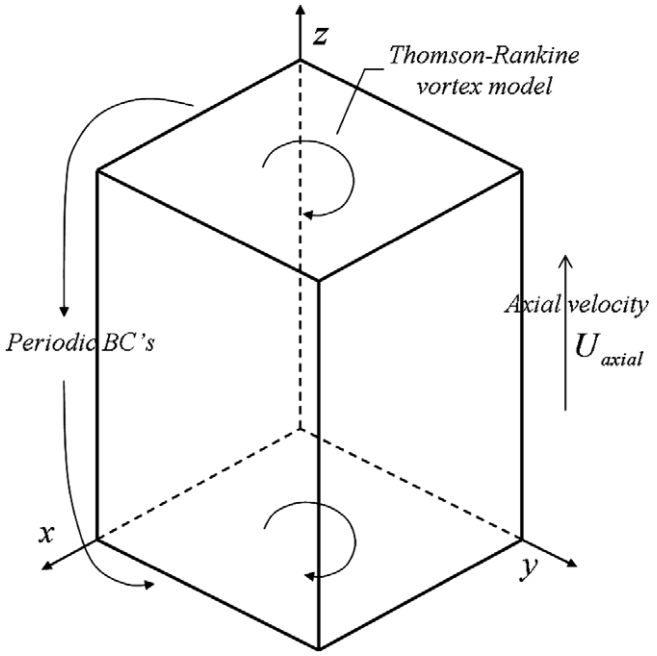

Fig. 16. Schematic diagram of passive vortex simulation.

Fig. 16 illustrates computational setup for the passive vortex simulation, which is similar to Hall and Long's simulation [31]. Computational domain covers from -1 to 1 along each coordinate direction with equal grid spacing, and grid system is $(50 \times 50 \times 50)$. Axis of the vortex is not aligned with any coordinate. Periodic boundary condition is applied. As a vortex model, the classical Thomson–Rankine model is adopted which is composed of the free vortex outside core, and the forced vortex inside the core. Initial condition is given by

(*a*) *Free vortex (outside the core)*: *if* $r > a$,

$$V_\theta = \frac{\omega a^2}{r}, \quad V_r = 0,$$

(*b*) *Forced vortex (inside the core)*: *if* $r \leqslant a$,

$$V_\theta = \omega r, \quad V_r = 0,$$

where V_θ and V_r are velocity components in cylindrical coordinate. Pressure and density distributions of the vortex are obtained from the simplified radial momentum equation and energy equation.

$$\frac{\mathrm{d}p}{\mathrm{d}r} = \frac{p}{\frac{p_0}{\rho_0} - \frac{\gamma-1}{2\gamma}(V_\theta^2 + U^2)} \frac{V_\theta^2}{r},$$

where U is axial velocity. (p_0, ρ_0) is stagnation pressure and density, respectively. By integrating the equation from vortex center to outside, all the property distributions can be obtained.

Figs. 17 and 18 shows initial density contour and computed results of five different methods at the non-dimensional time of $t = 20$. Compared to the initial distribution, results by minmod and van Leer limiters are somewhat diffused, while vortex structure by superbee limiter is completely fallen apart due to over-compression. On the other hand, the results by MLP seem to maintain the core profile accurately. For more quantitative comparison, density distributions passing through vortex core are compared in Fig. 19. Result by the

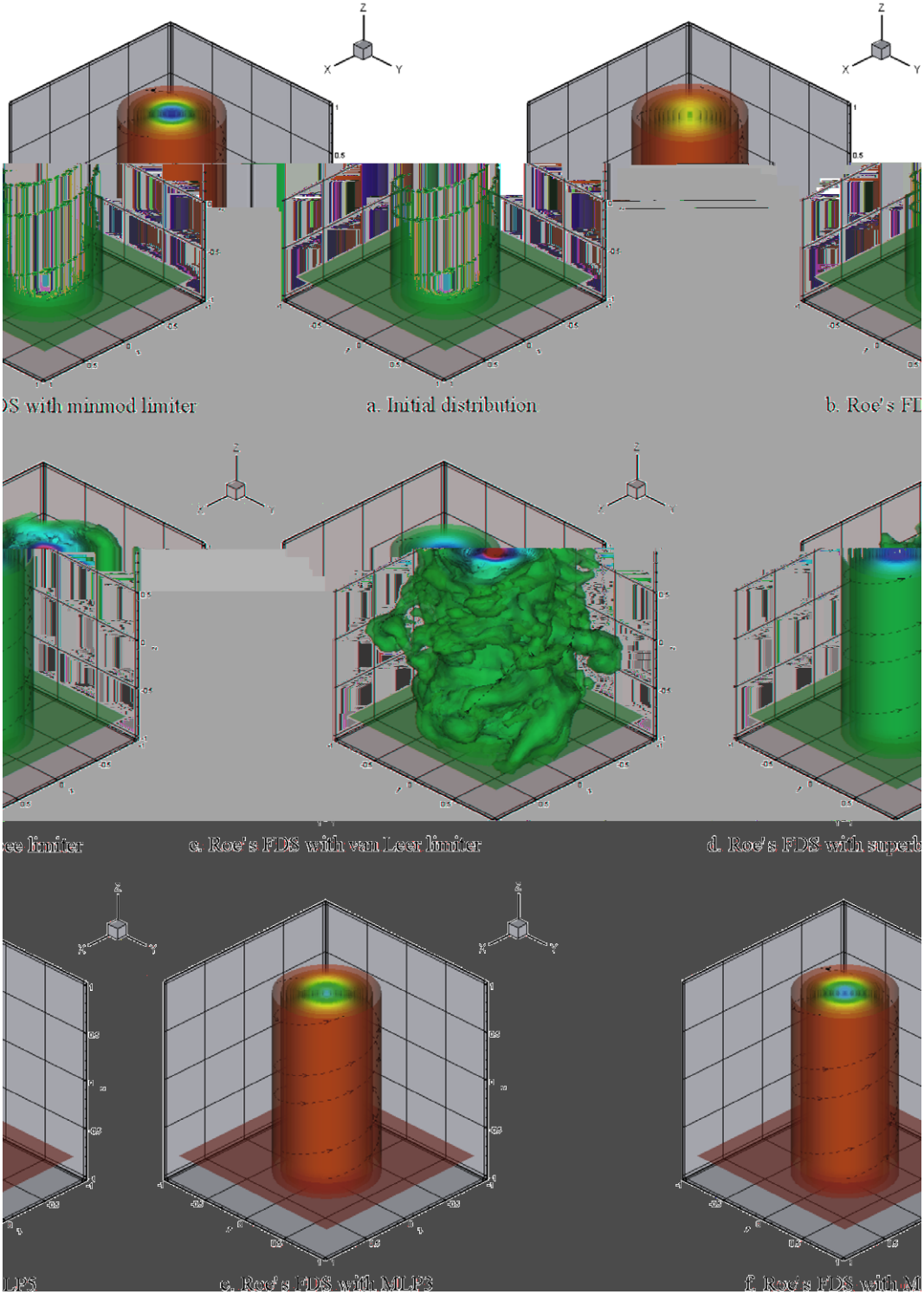

Fig. 17. Density contour and iso-surface of passive vortex simulation with non-inclined vortex center axis. Third order TVD Runge–Kutta method is used. Computed results at $t^* = 20$.

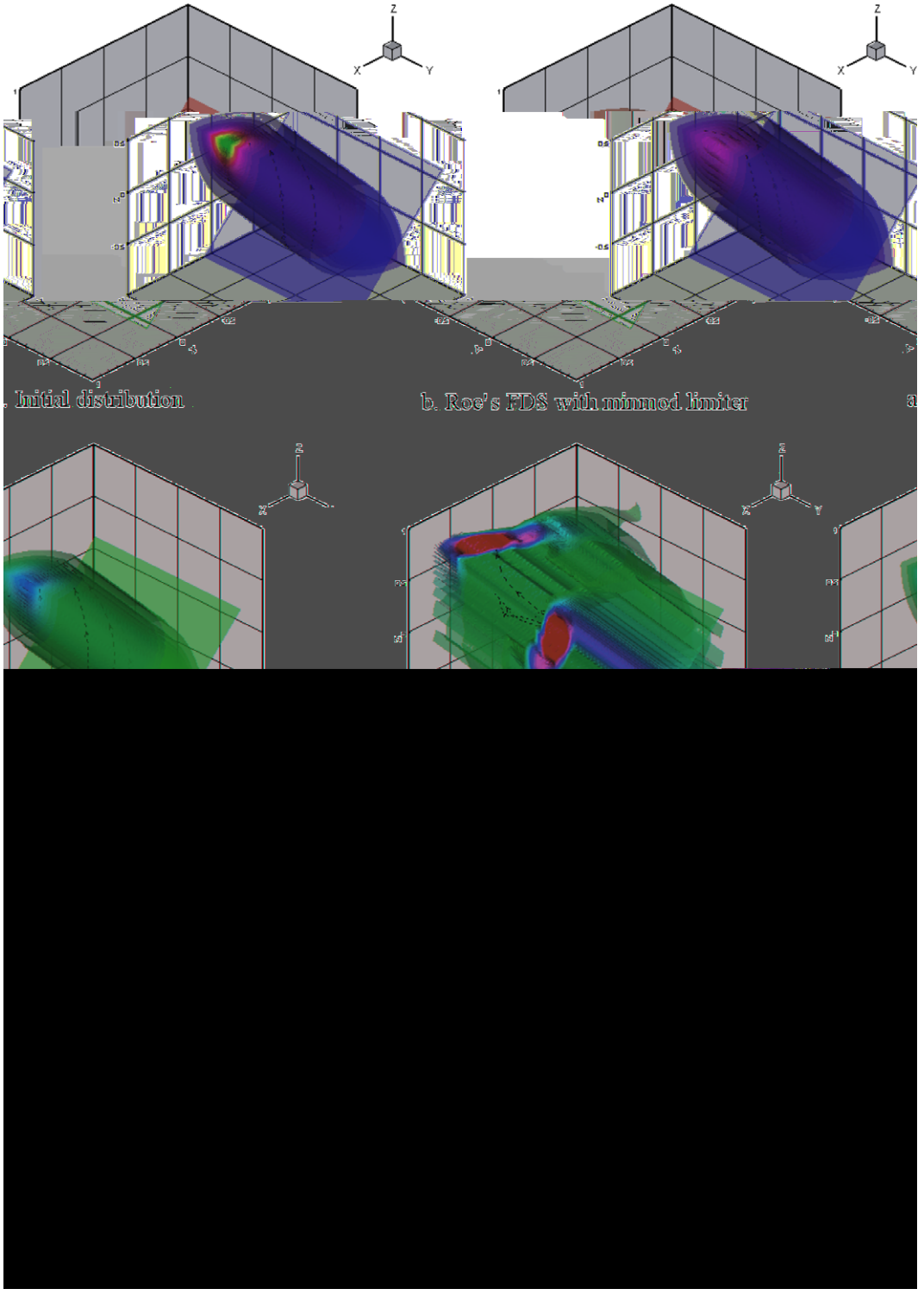

Fig. 18. Density contour and iso-surface of passive vortex simulation with inclined vortex center axis. Third order TVD Runge–Kutta method is used. Computed results at $t^* = 20$.

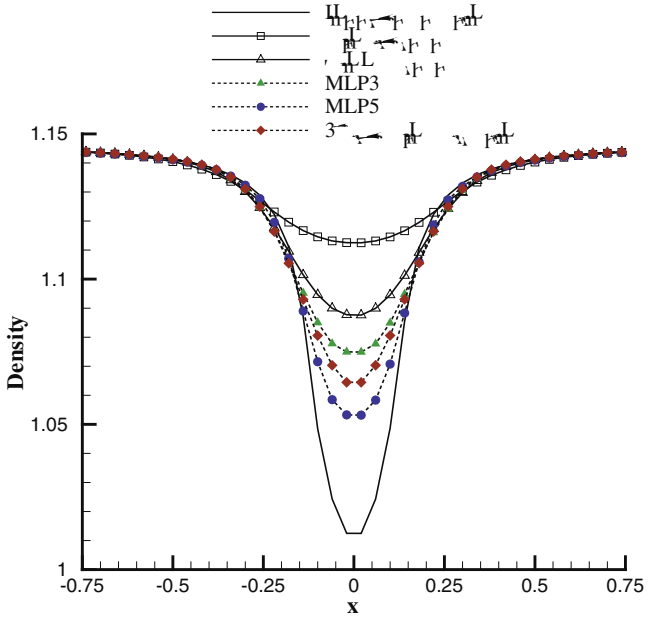

Fig. 19. Comparison of density distribution along the x-direction. $y = z = 0.0$. The result by the third order interpolation without any limiting is added for the purpose of accuracy comparison.

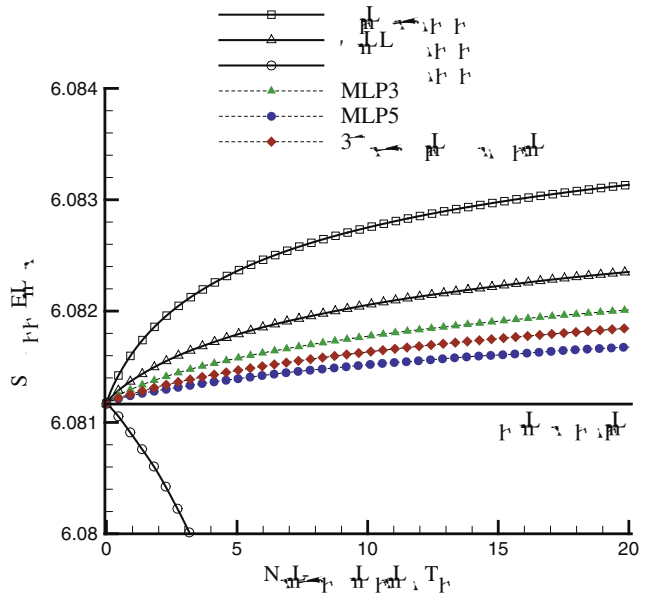

Fig. 20. Comparison of specific entropy for passive vortex simulation. Isentropic line corresponds to the exact solution.

third-order interpolation without any limiting is added for the purpose of accuracy comparison. MLP3 is very much comparable to the third-order interpolation without limiting, and MLP5 yields more accurate result.

Fig. 20 is comparison of entropy production according to each interpolation scheme. In case of superbee limiter, entropy decreases without lower bound due to over-compression. As a result, computed solution becomes unstable and computation fails. On the other hand, MLP5 yields the least increase of entropy among interpolation schemes.

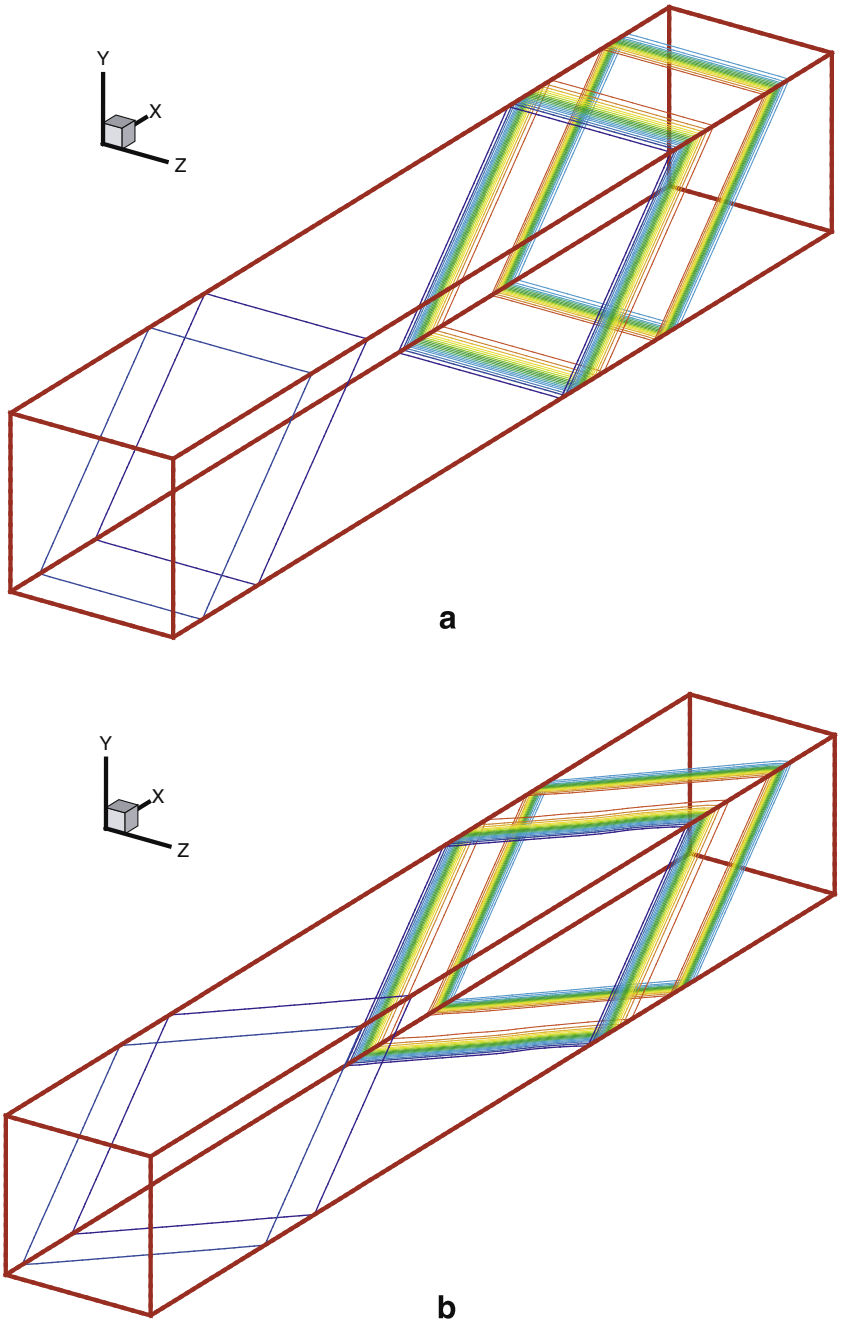

4.7. Three-dimensional oblique Lax's shock-tube problem

Similar to oblique Sod's shock-tube problem [5,7,30], one-dimensional Lax's shock-tube problem is implemented in three-dimensional setting with non-aligned grid directions. This is to examine capability of numerical schemes in resolving waves that are oblique to computational mesh.

Initial jump condition makes an angle θ in the x-axis, and ψ in the z-axis $(0 < \theta \leqslant \frac{\pi}{2}, 0 \leqslant \psi < \frac{\pi}{2})$. If $\theta = \frac{\pi}{2}$ and $\psi = 0$, we have one-dimensional situation. Otherwise, all the waves are oblique with respect

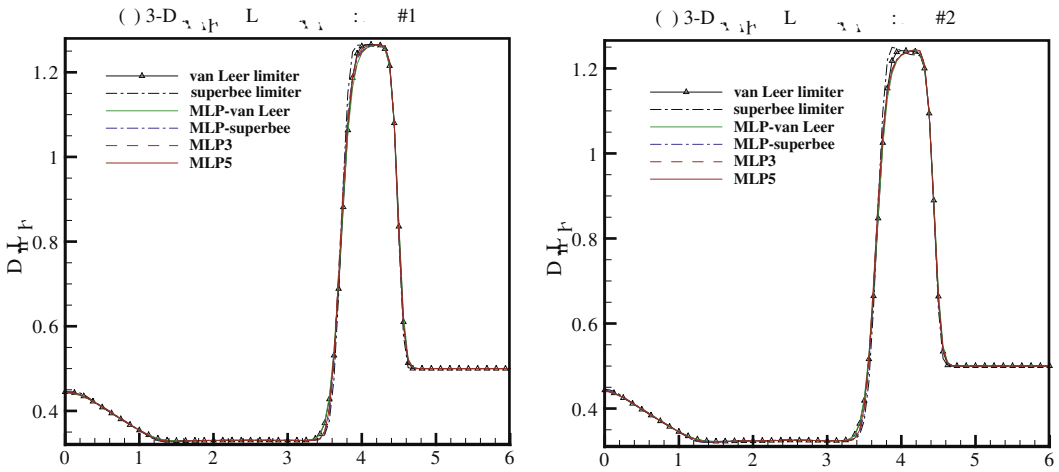

Fig. 22. Comparison of density distribution along x-axis at $y = 0$ and $z = 0$: (a) $\theta = \arctan 1$ and $\psi = 0$ and (b) $\theta = \arctan 1$ and $\psi = \arctan 1$.

to computational grid. We perform two test cases: Case1. $\theta = \arctan 1$ and $\psi = 0$ which belongs to a two-dimensional oblique Lax's problem, Case2. $\theta = \arctan 1$ and $\psi = \arctan 1$ which belongs to a three-dimensional oblique Lax's problem (see Fig. 21). Computational domain is $[0, 12] \times [0, 1] \times [0, 1]$, and grid size is equally spaced with $h = \frac{1}{16}$. Initial jump is located at $(x, y, z) = (5, 0, 0)$, and computation is carries out up to $t = 1.3$.

In Fig. 22, we compare density distributions obtained by conventional TVD MUSCL limiter and present method. All MLP-combined methods are doing well in resolving the three waves, but slight oscillation can be observed in Case2 from conventional TVD limiters. For more quantitative comparison, we display the difference between one-dimensional shock-tube result and three-dimensional counter part for each algorithm in Fig. 23. It can be seen that MLP3 and MLP5 perform similarly, while conventional TVD limiters and MLP-superbee give slight oscillations near discontinuity (see Figs. 22b and 23b). For this test case, overall performance of MLP is acceptable, and MLP controls spurious oscillation effectively. This confirms again that oscillation control mechanism of present method does not originate from excessive numerical dissipation.

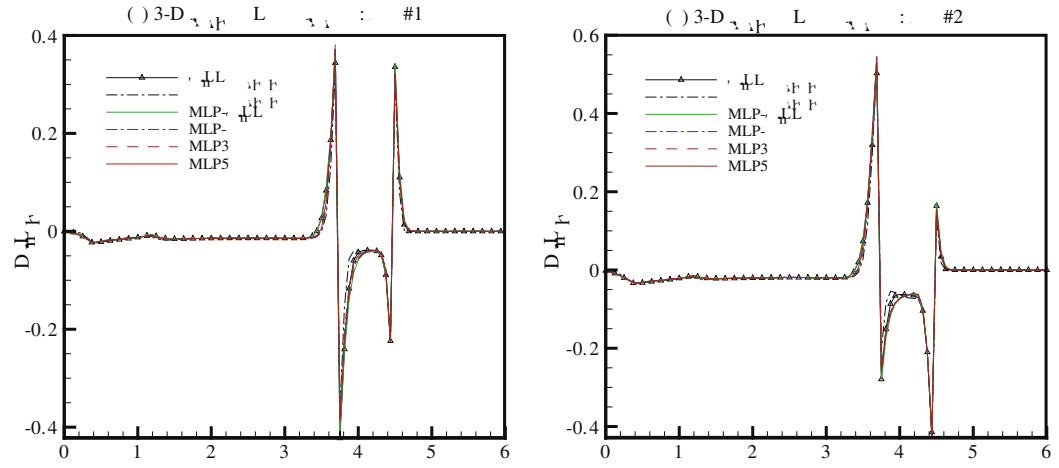

Fig. 23. Comparison of density difference from exact one-dimensional solution, $\rho - \rho_{1D}$, along x-axis at $y = 0$ and $z = 0$: (a) $\theta = \arctan 1$ and $\psi = 0$ and (b) $\theta = \arctan 1$ and $\psi = \arctan 1$.

4.8. Inviscid supersonic corner flow

Supersonic corner flow is usually defined as a high-speed flowfield over two intersecting surfaces. This flow can be observed in fuselage-wing junction, fin-wing junction, engine intake and so on. Since the first numerical analysis carried out by Kutler [32], many researchers have studied various corner flows [33–36]. Primary interests are surface flow pattern, complicated shock structure, pressure and heat transfer prediction, and so on.

Here, we consider a box-type inlet that is composed of two-intersecting wedges as shown in Fig. 24. Sweep angle of the leading edge $\chi = 0^\circ$, and the angle between the two leading edges $v = 90^\circ$ in the xy-plane. Flow structure changes according to the freestream Mach number and the wedge angle θ_w. In this work, cases of $M = 3.0, 6.0$ with zero angle of attack and $\theta_w = 10^\circ, 20^\circ$ are tested. As indicated in Fig. 24, the main purpose of this test is to examine the capability of capturing complex shock structure. In numerical simulation, all discontinuities including shock waves, slip surfaces, and interaction between three shocks and a slip surface are to be captured without spurious oscillation.

Fig. 25 shows comparison of pressure distribution at lower wall in case of $M = 3.0$ and $\theta_w = 10^\circ$. Conventional superbee and van Leer limiters show noticeable spurious oscillation which does not seem to be eliminated completely even with MLP version limiters. Compared to minmod limiter, MLP5 provides a completely monotonic result with much less numerical dissipation. Fig. 26 shows behavior of convergence history in each case. Cases of superbee and van Leer limiters are never converged. Even MLP-superbee does not show satisfactory performance due to visible pressure oscillation across the shock wave. On the other hand, MLP-van leer and MLP5 show good convergence characteristics. Though not presented here, similar results can be obtained for other flow conditions.

In order to verify the ability of capturing complex shock structure, the case of $M = 6.0$ and $\theta_w = 20^\circ$ is considered. This flow condition produces irregular reflection of shock waves and a spiral curl inside. Fig. 27 shows images of numerical schlieren using TVD MUSCL limiters and MLP. Spurious oscillation is produced again in cases of van Leer and superbee limiters (Fig. 27b and c). MLP-superbee limiter relieves oscillations around the mach stem, slip surface and spiral curl but does not eliminate them clearly. Minmod limiter gives a monotonic shock profile, but the slip line and spiral curl are very much diffused. On the other hand, MLP-van Leer and MLP5 provide more detailed structure. Slight wiggles are observed near the main mach stem, but they are too weak to influence the entire flowfield and convergence characteristics.

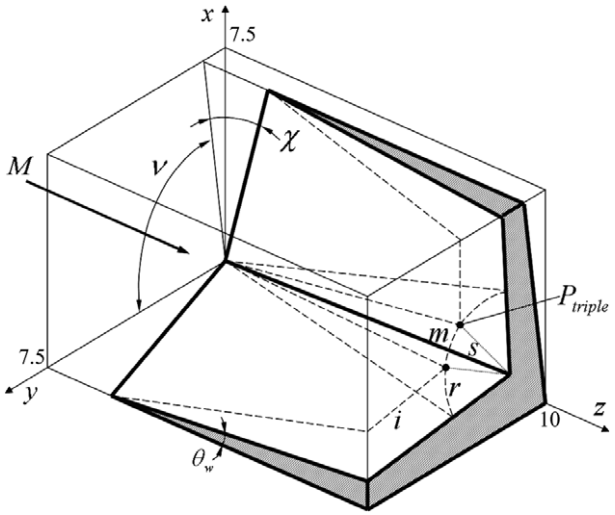

Fig. 24. Configuration of supersonic corner flow. Dashed line illustrates typical flow structure which is self-similar along the z-direction: m – mach stem, i – incident shock, r – reflected shock, s – slip line, P_{triple}-triple point.

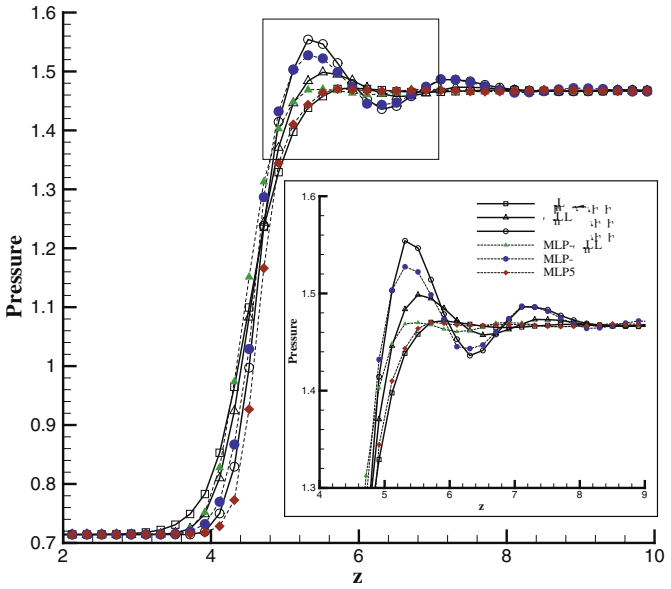

Fig. 25. Comparison of pressure distribution along the z-direction on lower wall ($M = 3.0$ and $\theta_w = 10^\circ$, $x = 0.0$ and $y = 7.5$).

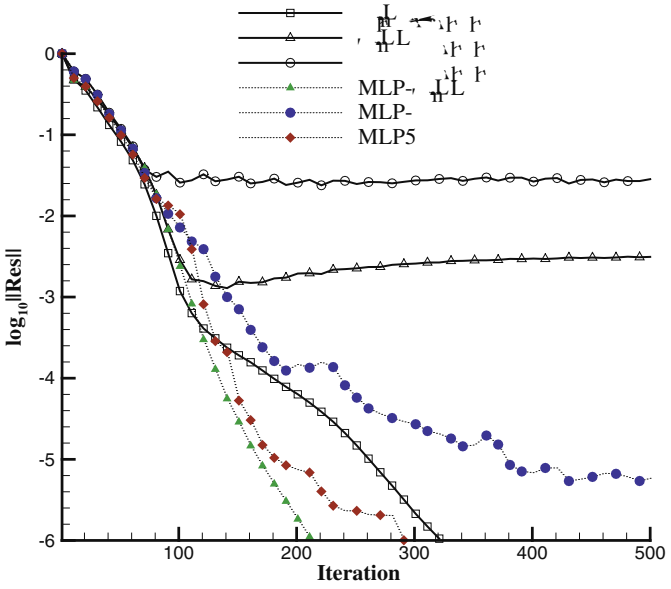

Fig. 26. Convergence history of six limiting methods for inviscid supersonic corner flow ($M = 3.0$ and $\theta_w = 10^\circ$). CFL number is 3.0 and LU-SGS is used.

4.9. Three-dimensional viscous shock-tube problem

Owing to complex flow structure involving interaction of shock wave, boundary layer and vortices, the two-dimensional viscous shock-tube problem has been popularly used to access performance of high-resolution numerical methods [37,38,16]. For a unit length square shock tube with insulated wall, a membrane located at $x = 0.5$, separates two different states of ideal gases. Initially, the membrane is removed and wave interaction begins. Due to viscous effect, wave interacts with horizontal wall, creating a thin boundary layer. After reflecting from the right end wall, the shock wave interacts with the thin boundary layer, changing flow pattern

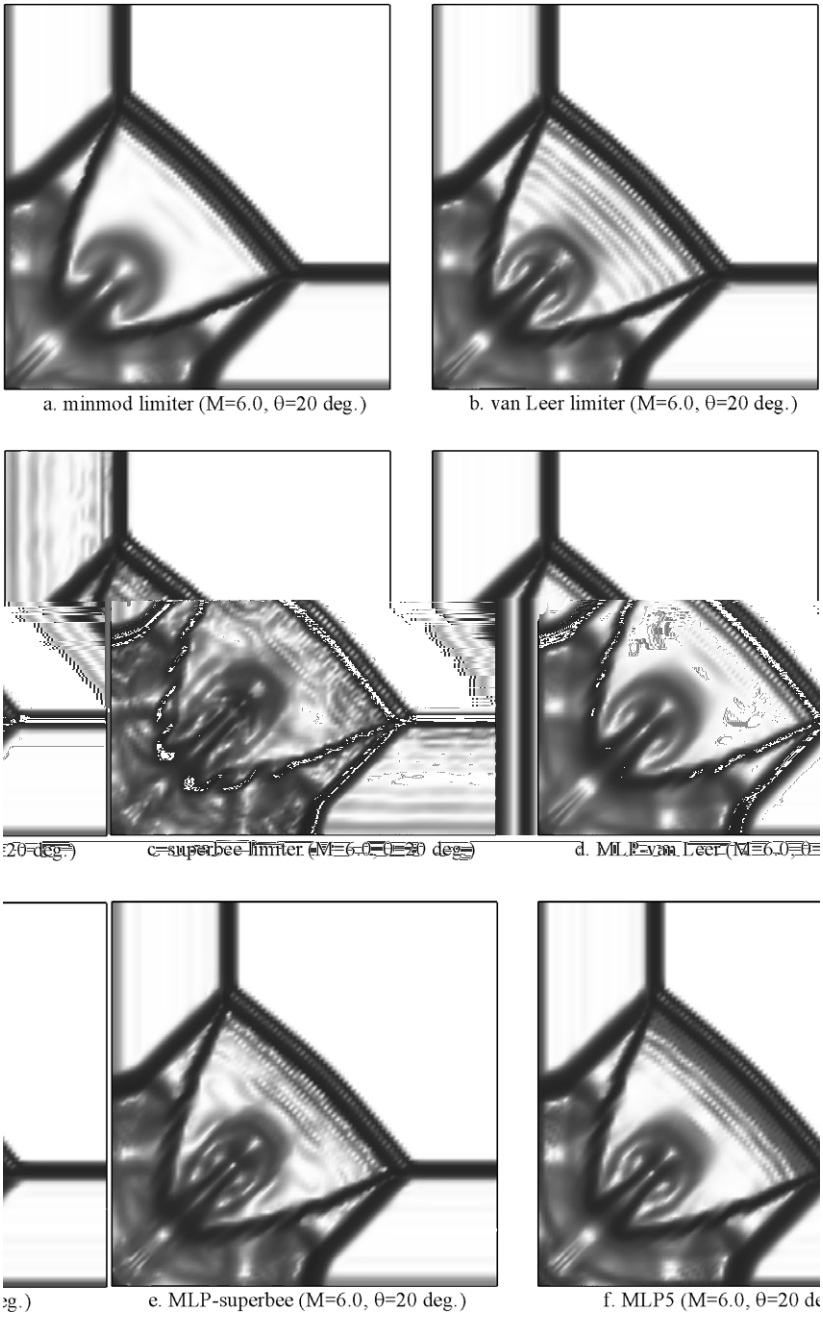

Fig. 27. Numerical scheliren of corner flow in the xy-plane (100×100 grid system, $M = 6.0$ and $\theta_w = 20^\circ$). RoeM [25] is used as a numerical flux function.

near horizontal wall. As a result, complex two-dimensional shock wave/boundary-layer interaction, including λ-shape shock wave and various sizes of vortices, is developed.

In the present work, the two-dimensional shock-tube problem proposed by Daru and Tenaud [37] is extended to three-dimensional case since another wall effect may provide more complex but interesting flow physics. In addition, it could be used as a numerical test case to evaluate accuracy of high-resolution numerical schemes for three-dimensional unsteady viscous flows.

For a unit length cube with $0 \leqslant x, y, z \leqslant 1$, and a membrane ($yz$-plane) located at $x = 0.5$ (see Fig. 28), initial states are given as follows:

$$(\rho, u, v, w, p)_{\mathrm{L}} = (120, 0, 0, 0, 120/\gamma),$$
$$(\rho, u, v, w, p)_{\mathrm{R}} = (1.2, 0, 0, 0, 1.2/\gamma),$$

where subscript L and R indicate the left and the right state, respectively. The specific ratio of heat $\gamma = 1.4$ and the Prandtl number is 0.73. No slip boundary with adiabatic wall condition is applied, and the Reynolds number is 200 with constant viscosity. M-AUSMPW+ [26] combined with MLP is compared with AUSMPW+ [27] combined with conventional TVD MUSCL limiters. Viscous fluxes are calculated by the fourth-order

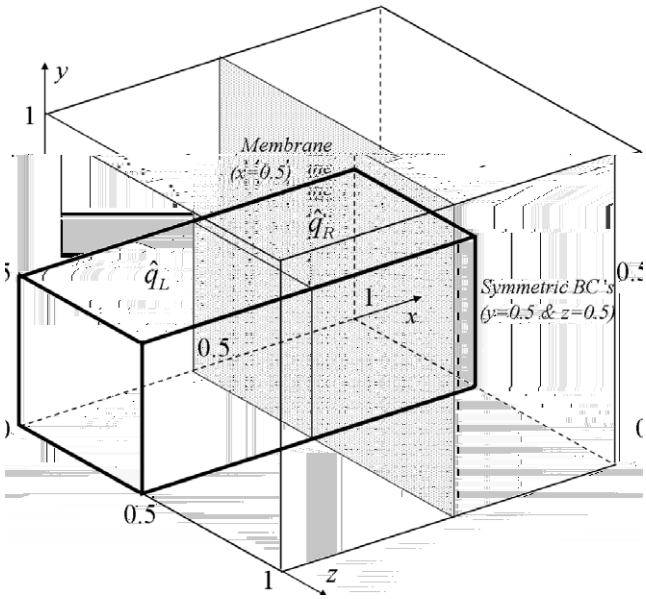

Fig. 28. Schematic diagram of three-dimensional viscous shock-tube problem.

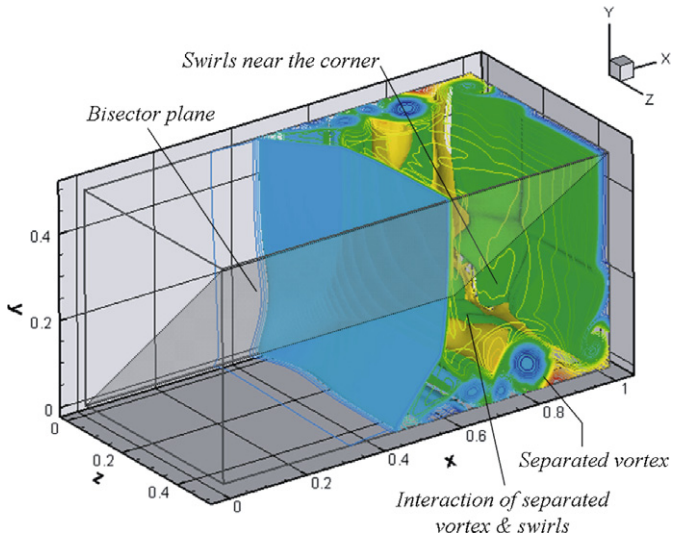

Fig. 29. Computed result of three-dimensional viscous shock-tube problem: density contour and iso-surface at $t^* = 1.0$.

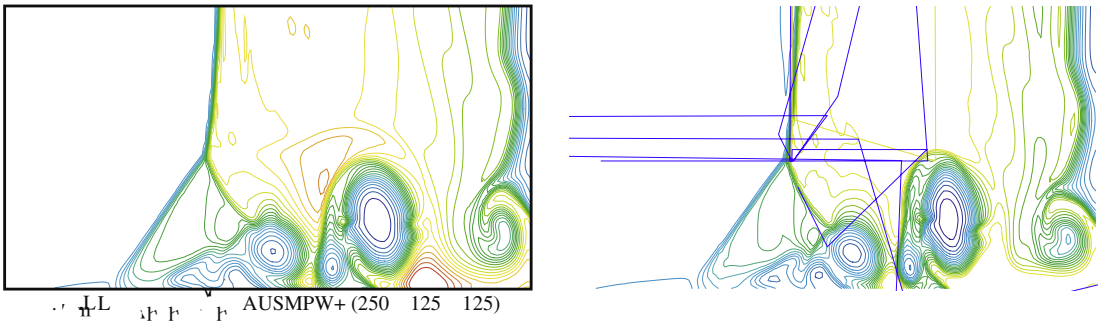

spatial accuracy, and the third-order accurate TVD Runge–Kutta method is used for time integration. MPI parallel computation is performed on PC clusters using 32 processors.

Fig. 29 shows density contour and iso-surface of computed results. Basically, three distinct flow features can be observed. First of all, flow pattern at symmetric plane is identical to the two-dimensional case in which the primary vortex is developed by the interaction of shock wave/boundary-layer interaction. Secondly, near corner of walls, various sizes of spiral curls are developed. Finally, spiral curls interact with a pillar-vortex near corner of walls.

In Fig. 30, density contours at symmetric plane (xy-plane at $z = 0.5$) are compared with three levels of grid refinement. Result of AUSMPW+ with van Leer limiter is used as a reference solution. Judging from the size and rotation angle of vortices, and the location of the λ-shock triple point, MLP5 with M-AUSMPW+ on coarse grid system ($250 \times 125 \times 125$) shows almost the same result with van Leer limiter with AUSMPW+ on medium grid system ($350 \times 175 \times 175$), which has 2.74 times more grid points. Also, MLP on medium grid system provides a very competitive result compared to van Leer limiter with AUSMPW+ on fine grid system ($500 \times 250 \times 250$), which has 2.915 times more grid points. Judging from the straightforward comparison, MLP5 with M-AUSMPW+ gives about three times grid reduction effect. Considering the fact that time stepping (or iteration number) is usually proportional to grid size in unsteady calculation, total computational cost saved by MLP5 with M-AUSMPW+ looks more than three times.

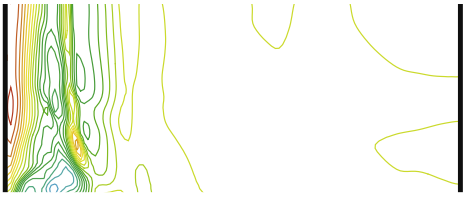

AUSMPW+ (250 125 125)

M-AUSMPW+ (250 125 125)

AUSMPW+ (350 175 175)

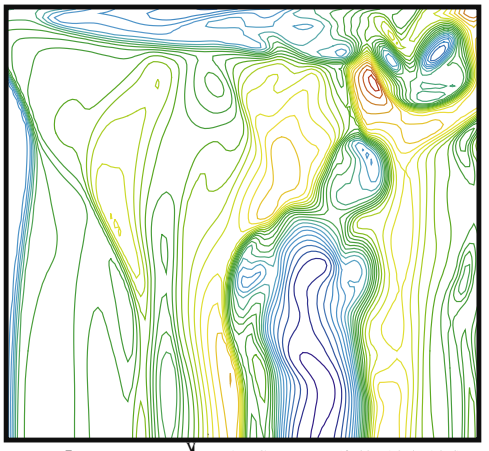

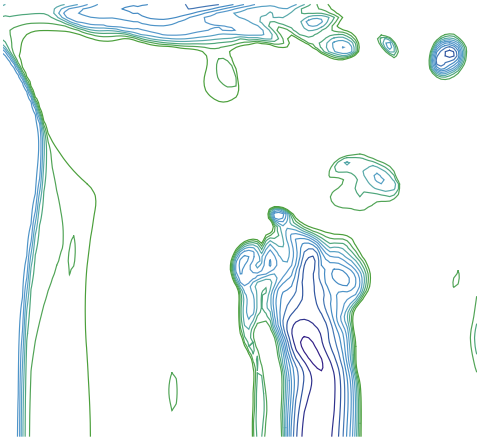

AUSMPW+ (350 125 125)

As the second flow feature, Figs. 31 and 32 show spiral curls in yz-plane at $x = 0.842, 0.8725$, respectively. As shown in Fig. 31c, d, depending on the amount of numerical dissipation, size and structure of spiral curls are substantially different. In Fig. 32c, small vortices, which are completely smeared out in van Leer limiter with AUSMPW+, are clearly captured by MLP even on coarse gird system. Superior performance of MLP over conventional limiting can be confirmed again.

As the last comparison, Fig. 33 shows interaction of spiral curls with the pillar-vortex. The primary separated vortex in two-dimensional flow, which can be seen in Fig. 30, forms a vortex pillar in three-dimensional

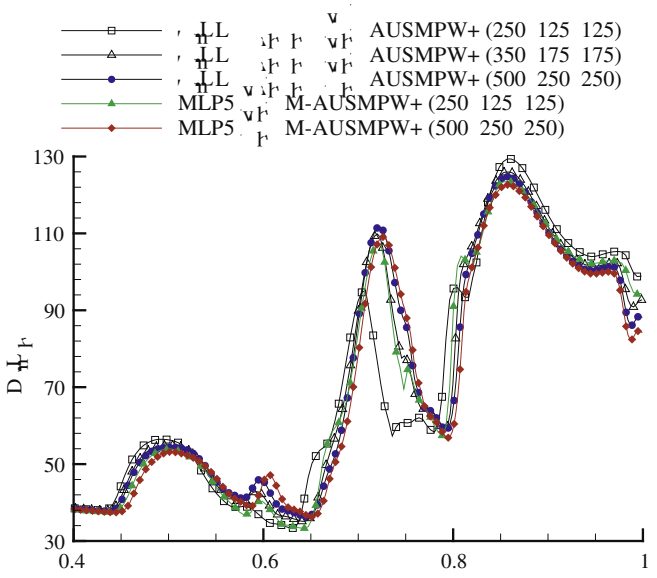

Fig. 34. Comparison of density distribution along the x-direction at $y = 0.0$ and $z = 0.5$, which corresponds to the lower wall in Fig. 30. Computed results are consistent to those of two-dimensional viscous shock-tube problem in Ref. [16].

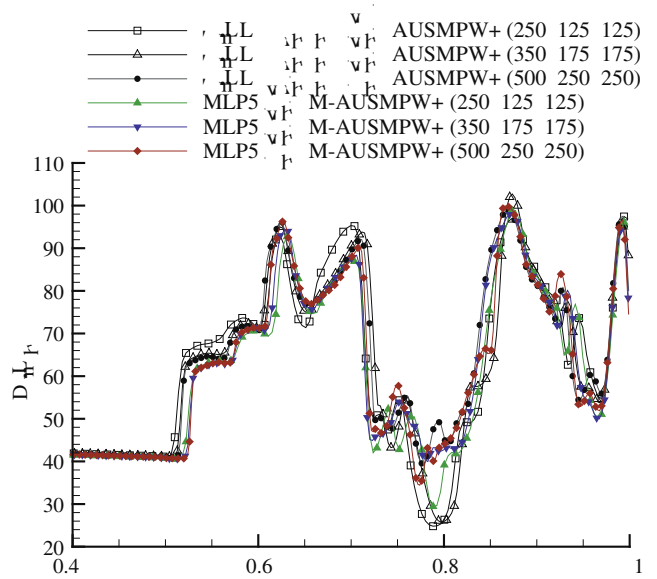

Fig. 35. Comparison of density distribution along the x-direction at $y = 0.078$ and $z = 0.25$, which crosses the pillar-shaped vortex in Fig. 33.

case. The small vortex, separated from the pillar-vortex due to interaction between the pillar-vortex and spiral curls, is clearly captured by MLP5 with M-AUSMPW+ on coarse grid system, while conventional limiting does not provide the flow feature even on medium grid system.

For more quantitative comparison, density distributions near the primary vortex and at the end of the pillar-shaped vortex are examined in Figs. 34 and 35. As prior comparisons, the results by MLP on coarse grid system are closer to the fine grid solution.

Based on various test cases and comparisons, it is observed that MLP approach controls numerical oscillation quite effectively in multi-dimensional flows including both continuous and discontinuous regions, and as a result, solution accuracy and convergence characteristics are remarkably enhanced.

5. Conclusion

As a continual work on the multi-dimensional limiting process (MLP) which was successfully proposed in two-dimensional case, limiting strategy for three-dimensional compressible flows is developed by combining multi-dimensional limiting function with TVD interpolation.

For three-dimensional extension, formulation of MLP is newly derived for computational efficiency and easy implementation. Without assuming local constant gradient, the maximum and minimum cell-averaged values around a vertex point can be simply determined by employing *max* and *min* function. For efficient formulation, variation ratio is directly used instead of local gradient angle.

Through numerous test cases and careful comparisons, it is observed that the newly developed MLP maintains several desirable characteristics, such as multi-dimensional monotonicity and robust convergence both in discontinuous and continuous regions. From an optimal slope obtained by higher-order polynomial interpolation, MLP yields more accurate solutions compared to conventional limiting, which brings a significant grid reduction effect. Thanks to these properties, MLP combined with improved flux functions, such as Roe-type and AUSM-type schemes, can provide remarkable increase in accuracy, convergence and robustness both in steady and unsteady three-dimensional compressible flow.

Acknowledgments

The authors appreciate financial support by the Brain Korea-21 Program for the Mechanical and Aerospace Engineering Research at Seoul National University, and by the Korea Science and Engineering Foundation (Grant R01-2005-000-10059-0). This article was also granted by the Smart UAV Development of the 21th Frontier R/D Program sponsored by the Ministry of Commerce, Industry and Energy. We appreciate referees for careful comments and valuable suggestions.

References

[1] A. Harten, High resolution schemes for hyperbolic conservation laws, J. Comput. Phys. 49 (3) (1983) 357–393.
[2] P.K. Sweby, High resolution schemes using flux limiters for hyperbolic conservation laws, SIAM J. Numer. Anal. 21 (5) (1984) 995–1011.
[3] A. Harten, B. Engquist, S. Osher, Chakravarthy, Uniformly high order accurate essentially non-oscillatory schemes, J. Comput. Phys. 71 (1987) 231–303.
[4] C.W. Shu, S. Osher, Efficient implementation of essentially non-oscillatory shock-capturing schemes, J. Comput. Phys. 77 (1988) 439–471.
[5] J. Casper, C.-W. Shu, H.L. Atkins, Comparison of two formulations for high-order accurate essentially nonoscillatory schemes, AIAA J. 32 (1994) 1970–1977.
[6] Xu-Dong Liu, Stanley Osher, Tony Chan, Weighted essentially non-oscillatory schemes, J. Comput. Phys. 15 (1994) 200–212.
[7] Guang-Shan Jiang, Chi-Wang Shu, Efficient implementation of weighted ENO schemes, J. Comput. Phys. 126 (1996) 202–228.
[8] Dinshaw S. Balsara, Chi-Wang Shu, Monotonicity preserving weighted essentially non-oscillatory schemes with increasingly high order of accuracy, J. Comput. Phys. 160 (2000) 405–452.
[9] Chi-Wang Shu, Essential non-oscillatory and weighted essentially non-oscillatory schemes for hyperbolic conservation laws, NASA ICASE Report No. 97-65.
[10] C.W. Shu, TVB uniformly high-order schemes for conservation laws, Math. Comput. 49 (179) (1987) 105–121.
[11] A. Suresh, H.T. Huynh, Accurate monotonicity-preserving schemes with Runge–Kutta time stepping, J. Comput. Phys. 136 (1997) 83–99.

[12] H.C. Yee, N.D. Sandham, M.J. Djomehri, Low-dissipative high-order shock-capturing methods using characteristic-based filters, J. Comput. Phys. 150 (1999) 199–238.
[13] Eric Garnier, Pierre Sagaut, Michel Deville, A class of explicit ENO filters with application to unsteady flows, J. Comput. Phys. 170 (2001) 184–204.
[14] A. Jameson, Analysis and design of numerical schemes for gas dynamics 1 artificial diffusion, upwind biasing, limiters and their effect on accuracy and multigrid convergence, Int. J. Comput. Fluid Dyn. 4 (1995) 171–218.
[15] J.B. Goodman, R.J. LeVeque, On the accuracy of stable schemes for 2D scalar conservation laws, Math. Comput. 45 (1985) 15–21.
[16] K.H. Kim, C. Kim, Accurate, efficient and monotonic numerical methods for multi-dimensional compressible flows. Part II: Multi-dimensional limiting process, J. Comput. Phys. 208 (2) (2005) 570–615.
[17] B. van Leer, Toward the ultimate conservative difference scheme, J. Comput. Phys. 32 (1979) 101–136.
[18] S.P. Spekreijse, Multigrid solution of monotone second order discretizations of hypersonic conservations laws, Math. Comput. 49 (1987) 135–155.
[19] T.J. Barth, D. Jespersen, The design and application of upwind schemes on unstructured meshes, in: Proceedings of the 27th AIAA Aerospace Sciences Meeting, Reno, NV, 1989 (Paper AIAA 89-0366).
[20] T.J. Barth, P. Frederickson, Higher order solution of the Euler equations on unstructured grids using quadratic reconstruction, in: Proceedings of the 28th AIAA Aerospace Science Meeting, Reno, NV, 1990 (Paper AIAA 90-0013).
[21] Timothy Barth, Numerical methods for conservation laws on structured and unstructured meshes, VKI Lecture Series, 2003.
[22] V. Venkatakrishnan, Convergence to steady state solutions of the Euler equations on unstructured grids with limiters, J. Comput. Phys. 118 (1995) 120–130.
[23] Jianxian Qiu, Chi-Wang Shu, On the construction, comparison, and local characteristic decomposition for high-order central WENO schemes, J. Comput. Phys. 183 (2002) 187–209.
[24] P.L. Roe, Approximate Riemann solvers, parameter vectors, and difference schemes, J. Comput. Phys. 43 (1981) 357–372.
[25] S. Kim, C. Kim, O.H. Rho, S.K. Hong, Cures for the shock instability: development of a shock-stable Roe scheme, J. Comput. Phys. 185 (2003) 342–374.
[26] K.H. Kim, C. Kim, Accurate, efficient and monotonic numerical methods for multi-dimensional compressible flows. Part I: Spatial discretization, J. Comput. Phys. 208 (2) (2005) 527–569.
[27] K.H. Kim, C. Kim, O.H. Rho, Methods for the accurate computations of hypersonic flows, Part I: AUSMPW + Scheme, J. Comput. Phys. 174 (2001) 38–80.
[28] S. Yoon, A. Jameson, Lower-upper symmetric-Gauss–Seidel method for the Euler and Navier–Stokes equations, AIAA J. 26 (9) (1988) 1025–1026.
[29] P. Woodward, P. Colella, The numerical simulation of two-dimensional fluid flow with strong shocks, J. Comput. Phys. 54 (1984) 115–173.
[30] G.-S. Jiang, D. Levy, C.-T. Lin, S. Osher, E. Tadmor, High-resolution nonoscillatory central schemes with nonstaggered grids for hyperbolic conservation laws, SIAM J. Numer. Anal. 35 (6) (1998) 2147–2168.
[31] C.M. Hall, L.N. Long, High-order accurate simulations of wake and tip vortex flowfields, in: Proceedings of the 55th Annual Forum of American Helicopter Society, vol. 2, Alexandria, VA, May 1999.
[32] P. Kutler, Supersonic flow in the corner formed by two intersecting wedges, AIAA J. 12 (5) (1974) 577–578.
[33] J.S. Shang, W.L. Hangkey, Numerical solution of the Navier–Stokes equations for a three-dimensional corner, AIAA J. 15 (11) (1977) 1575–1583.
[34] F. Marconi, Supersonic, inviscid, conical corner flowfields, AIAA J. 18 (1) (1980) 78–84.
[35] R. Marsilio, Vortical solutions in supersonic corner flows, AIAA J. 31 (9) (1993) 1651–1658.
[36] Y.P. Goonko, A.N. Kudryavtsev, R.D. Rakhimov, Supersonic inviscid flows with three-dimensional interaction of shock waves in corners formed by intersecting wedges, in: Proceedings of the 11th International Conference on Methods of Aerophysical Research, Novosibirsk, Russia, 1–7 July 2002.
[37] V. Daru, C. Tenaud, Evaluation of TVD high resolution schemes for unsteady viscous shocked flows, Comput. Fluids 30 (2001) 89–113.
[38] B. Sjögreen, H.C. Yee, Grid convergence of high order methods for multiscale complex unsteady viscous compressible flows, J. Comput. Phys. 185 (2003) 1–26.